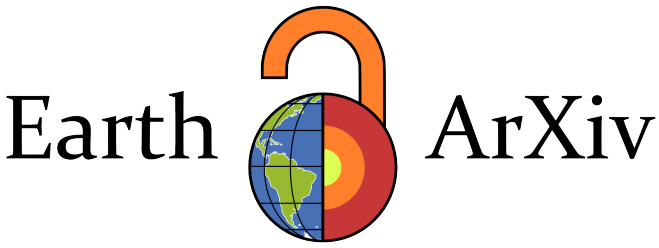

The article entitled “Reconstructing Land Surface Temperature for Cloud-Covered Regions: A Review of Methods” authored by Marwa Alfouly[1], Smajil Halilovic[1], Niklas Boers[2] and Thomas Hamacher[1]

[1]Chair of Renewable and Sustainable Energy Systems, Technical University of Munich, Germany.
[2]Professorship of Earth System Modelling, Technical University of Munich, Germany.

Reconstructing Land Surface Temperature for Cloud-Covered Regions: A Review of Methods

Marwa Alfouly, Smajil Halilovic, Niklas Boers, Thomas Hamacher

***Abstract*—Understanding surface thermal conditions is essential for studying ecosystem responses, hydrological processes, and climate-driven environmental change. Land Surface Temperature (LST) is a key parameter for studying a wide range of environmental and climatic processes. Although remote sensing technologies enable the acquisition of LST data on a global scale, satellite observations are frequently obscured by cloud cover, resulting in spatial and temporal data gaps that limit their usability. This work provides a comprehensive review of existing methods developed to reconstruct gap-free LST data. First, state-of-the-art methods are systematically reviewed and classified into rule-based and data driven methods. For each method, the underlying principles are explained, alongside details on implementation, validation, and the selected case study, providing critical insights into their performance and generalizability. Second, the growing potential of advanced methods—particularly deep learning frameworks—is explored, highlighting their adaptability for the task of LST gap-filling. The findings indicate that despite the development of sophisticated models, significant challenges remain, especially regarding the generalizability of the methods in varying climatic and urban environments. In addition, inconsistencies are identified in the evaluation metrics, limiting the direct comparability of the methods. This review can help guide future research efforts by highlighting current limitations and identifying promising directions for the development of more robust and adaptable LST gap-filling approaches.**

***Index Terms*—Land Surface Temperature (LST), Inpainting, Cloud cover, Remote sensing data gaps, Machine learning**

ABBREVIATIONS

ATC	Annual temperature cycle
BME	Bayesian maximum entropy
CCW	Correlation coefficient weighting
CDF	Cumulative distribution function
CFSDAF	Compressive Flexible spatiotemporal data fusion
CLM5.0	Community Land Model Version 5.0
CNN	Convolutional neural network
DCT	Discrete cosine transform
DDSDA	Differential Dynamic Search Distance
DINEOF	Data interpolating empirical orthogonal functions
EOF	Empirical Orthogonal Function
ERA5	The European Centre for medium-range weather forecasts reanalysis data, fifth generation
ESTARFM	Enhanced STARFM
EVI	Enhanced vegetation index
FFC	Fast Fourier convolution
EVI	Feed Forward Network
FSDAF	Flexible spatiotemporal data fusion
GAM	Generalized Additive model
GAN	Generative adverserial network
GBM	Gradient boosting machine
GLOSTFM	Global Spatiotemporal Fusion Model
HANTS	Harmonic Analysis of Time Series
IDW	Inverse distance weighting
IMA	Interpolation of the mean anomalies
INCA	Integrated Nowcasting through Comprehensive Analysis
ISFAT	Integrated spatiotemporal fusion algorithm
LaMa	Resolution-robust Large mask inpainting
LOTSFM	Long time-series spatiotemporal fusion model
LSM	Land surface models
LST	Land surface temperature
LSTM	Long-short term memory neural network
LWR	Local weighted regression
MINDEOF	Multivariate Data Interpolating Empirical Orthogonal Functions
MKF	Multi-resolution Kalman filtering
MMT	Multisensor Multiresolution Technique
MVC	Maximum value compositing technique
NDVI	Normalize difference vegetation index
NRN	Nonlocality-Reinforced Network
OK	Ordinary kriging
PLS	Penalized least square regression
PMW	Passive microwave sensors
RF	Random forest
RK	Regression kriging
RNN	Recurrent neural network
RSDAST	Remotely sensed daily land surface temperature reconstruction model
SADFAT	Spatiotemporal adaptive data fusion algorithm for temperature mapping
SAM	Simple arithmetic mean
SAPC2	Source augmented partial convolution model, Version 2
SEB	Surface energy balance
SFRFR	Spatial feature-considered random forest regression
SSA	Singular spectrum decomposition
STAN	Spatiotemporal attention network
STARFM	Spatial and temporal adaptive reflectance fusion model
STITFM	Spatio-Temporal Integrated Temperature Fusion Model

Corresponding author: Marwa Alfouly, marwa.alfouly@tum.de

Marwa Alfouly, Smajil Halilovic, and Thomas Hamacher are with the Chair of Renewable and Sustainable Energy Systems, Technical University of Munich, Germany.

Niklas Boers is with the Professorship of Earth System Modelling, Technical University of Munich, Germany.

STRF	Spatial-temporal random forest
SUHI	Surface urban heat island
SVD	Singular vector decomposition
SVR	Support vector regression
TIR	Thermal infrared sensors
TPS	Thin plates spline
TSIP	Two-step improved similar pixels
UHI	Urban heat island
XGBoost	Extreme gradient boosting

I. Introduction

LAND and Surface Temperature (LST) is a fundamental component of the Earth's climate system influncing the exchange of energy and water between the land surface and the atmosphere [1], [2]. Its influence spans numerous scientific domains. It is a key indicator for monitoring global ecosystem health, detecting vegetation stress, and evaluating the severity of agricultural droughts [3]. In addition, LST datasets are essential inputs for numerical weather prediction [4], [5], regional climate modelling [6], and hydrological forecasting [7], [8]. Furthermore, it is a critical metric for assessing and monitoring urban heat islands (UHIs) —urban areas that experience significantly higher temperatures than their rural surroundings [9]. Reiners et al. [10] provide an extensive overview of the applications of LST in the context of global change.

Remote sensing has proven to be the most effective method for retrieving LST, utilizing passive microwave sensors (PMW) or thermal infrared sensors (TIR). These technologies enable accurate and large-scale surface temperature monitoring, delivering the high-value information required for modelling surface–atmosphere interactions, diagnosing thermal anomalies, and evaluating climate-related risks. However, both sensor types have inherent limitations that hinder direct, consistent LST measurement. High spatial and temporal resolution, along with cloud-free conditions, are crucial for reliable data but are often challenging to achieve. Passive microwave sensors can penetrate cloud cover and provide LST estimates even in cloudy conditions; however, they suffer from coarse spatial resolution. On the other hand, TIR sensors offer fine spatial resolution, but their measurements are compromised by cloud cover, resulting in missing data for cloudy pixels. These trade-offs between spatial resolution and data continuity hinder the accurate representation of surface temperature variability across diverse environments and reduce the effectiveness of subsequent environmental analyses. Table I summarizes the available LST resources and their corresponding features, highlighting these key challenges.

As a result, significant efforts have been directed towards the generation and validation of high spatiotemporal resolution LST data [12]. These efforts have increasingly focused on the filling and reconstruction of cloud-contaminated images, aiming to recover missing or obscured LST information. Reconstruction methods developed up to 2020 have been reviewed in [13], [14]. Since then, machine learning has made substantial contributions to advancing LST reconstruction techniques. This paper reviews and evaluates the existing methods for generating complete LST datasets, and explores transferable image processing techniques from related domains that may enhance LST reconstruction. By extending prior surveys, this review systematically integrates machine learning and physics-enhanced LST reconstruction methods developed since 2020. It introduces a unified methodological taxonomy and critically compares reconstruction methods across diverse validation strategies, revealing inconsistencies in benchmarking practices and limitations in generalizability. By highlighting challenges in cross-climatic and cross-scale transferability, the review outlines key directions for developing robust, next-generation gap-filling frameworks.

The paper is organized as follows. Section II establishes the theoretical foundation, detailing the physical principles governing LST alongside an overview of key machine learning concepts applied in modern reconstruction methods. Section III provides a comprehensive review of state-of-the-art gap-filling and fusion methodologies; including a comparative analysis of their reported performance accuracies across diverse terrains. In Section IV, we synthesize these findings through a critical discussion of methodological limitations and emerging research directions, with a focus on key concepts and insights from each previously defined category. Finally, conclusions are presented in Section V.

II. Theortical Background

A. Physics

LST is a key physical parameter that represents the Earth's radiative skin temperature and provides a quantitative measure of its surface thermal state. As a physical quantity, its estimation is governed by the laws of thermodynamics, particularly the conservation of energy. While data-driven methods can be powerful, they have no inherent knowledge of these physical laws. Therefore, a physics-based framework can guide the estimation, constrain the model outputs, and ensure the reconstructed LST is physically plausible. This section outlines the physical foundations underlying physics-constrained hybrid LST reconstruction methods.

At the core of this foundation lies the Surface Energy Balance (SEB), which represents the conservation of energy at the land surface. The SEB describes the balance between the energy reaching and leaving the ground surface through net radiation, and the corresponding ground and turbulent fluxes, storage, and metabolic terms [15]. Quantitative knowledge of the SEB is essential for the prediction of weather and climate [16]. The SEB is expressed by the following core equation [16], [17]:

$$R_n = H + LE + G + Imb \tag{1}$$

which represents the available net radiation (R_n) as the sum of the sensible heat flux (H), the latent heat flux (LE), and the ground heat flux. The imbalance (Imb) is considered as the total contribution of neglected effects and uncertainties. Under given surface conditions, the sensible heat flux is primarily determined by the surface temperature and the meteorological conditions at the reference height and is not constrained by the available energy [18]. The SEB estimates LST by balancing energy inputs and outputs. In numerical models, such as that

TABLE I
REMOTE SENSING LST DATASETS

	Dataset	Spatial resolution	Revisit	Spatial Coverage
TIR	NOAA/AVHRR[1]	1.1 km - 4 km	Daily	Global
	MODIS[2]	1 km	Daily	Global
	VIIRS[3]	750 m	Daily	Global
	Sentinel-3	1 km	Daily	Global
	Landsat-8/9	30 – 100 m	16 days	Global (excluding Poles)
	MSG SEVIRI[4]	3 km	15 minutes	Geostationary (Europe, Africa, Middle East)
	GOES[5]	2 km (ABI LST)	Hourly	Geostationary (Western Hemisphere)
	FY-2F/G[6]	5 km	Hourly	Geostationary (China)
	FY-3B/D[6]	250 m - 1 km	12 hours	Global
	Himawari-8	2 km	10 minutes	Geostationary (Japan/Oceania)
	ECOSTRESS[7]	70 m	1 — 5 days	Near-Global Land (52° N to 52° S)
	ASTER[8]	90 m	16 days	Global
PMW	GPM[9] LST	10 km	3 hours	Near-Global (approx. 65° N to 65° S)
	AMSR-E[10] LST	25 km	2 days	Global
	AMSR2[10] LST	10 km	2 days	Global
	SMOS[11] LST	40 — 50 km	2 — 3 days	Global

[1]NOAA/AVHRR: National Oceanic and Atmospheric Administration/The Advanced Very High Resolution Radiometer, [2]MODIS: Moderate Resolution Imaging Spectroradiometer, [3]VIIRS: Visible Infrared Imaging Radiometer Suite, [4]SEVIRI: Spinning Enhanced Visible and Infra-Red Imager, [5]GOES: Geostationary Operational Environmental Satellite, [6]FY-2/3: FY is Fengyun (China's weather satellite program), the number (2 or 3) indicates the satellite generation/type, and the letter (B, D, F, G, etc.) identifies the specific satellite within that series. [7]ECOSTRESS: ECOsystem Spaceborne Thermal Radiometer Experiment on Space Station [11], [8]ASTER: Advanced Spaceborne Thermal Emission and Reflection Radiometer, [9]GPM: Global Precipitation Measurement, [10]AMSR-E/2: Advanced Microwave Scanning Radiometer (for EOS/2), [11]SMOS: Soil Moisture and Ocean Salinity.

of the European Center of Medium-Range Weather Forecasts (ECMWF) [19], computed values of R_n, H, and LE, assuming that the residual is G, are used to determine the surface temperature equation with an iterative approach [17].

Building directly on this SEB principle, Land Surface Models (LSMs) are inherently physical models that are designed to numerically solve the SEB equation by simulating the complex interactions and feedback loops governing energy and water fluxes. The scientific conception of LSMs has undergone a profound evolution. Over the past several decades, they have transformed from rudimentary, oversimplified schemes into highly complex models that are central to Earth System science [20]. Most popular and well-documented LSMs are summarized in Table II [21]. In the context of LST reconstruction, LSMs serve two primary functions. First, they provide a physically consistent, continuous simulation of LST that can be used as a baseline for validation. For example, Koch et al. [22] utilized three LSMs from the North American Land Data Assimilation System Phase 2 (NLDAS-2) to simulate LST, which was then validated against a 30-year (1979–2009) remotely sensed LST dataset. Second, and more central to this review, LSMs serve as the physical engine in data assimilation and fusion frameworks. In this approach, the model is not just a simulator but is actively constrained by satellite observations to correct its estimates. Ghent et al. [23], for instance, used this method to constrain JULES model simulations with remotely sensed LST data from SEVIRI, thereby reducing inherent model uncertainty. This principle is the foundation for physics-enhanced methodsdiscussed in III-E, such as the fusion of satellite-derived LST (e.g., Landsat, MODIS) with CLM-simulated LST to generate a single, gapless, high-resolution product [24].

TABLE II
OVERVIEW OF COMMONLY USED AND WELL-DOCUMENTED LAND SURFACE MODELS (LSMS).

Model	Description / Notes
Noah LSM (Unified Noah)	Widely used operational LSM for weather and hydrological forecasting; includes soil moisture, vegetation, and snow processes.
HTESSEL	The Hydrology Tiled ECMWF Scheme for Surface Exchanges over Land; operational LSM of ECMWF, featuring tiled land surface representation and advanced soil hydrology.
BATS	The Biosphere–Atmosphere Transfer Scheme; early-generation LSM describing vegetation–atmosphere exchanges of heat, moisture, and momentum.
CLASS	The Canadian Land Surface Scheme; includes multilayer soil physics, snow processes, and vegetation parameterizations.
Noah-MP	The Community Noah Land Surface Model with Multi-Parameterization Options; offers flexible physics options for vegetation, soil, snow, and runoff processes.
CLM5	Community Land Model version 5; advanced, process-based LSM with multilayer canopy, soil biogeochemistry, hydrology, and energy balance schemes.
JULES	Joint UK Land Environment Simulator; physically based energy–water–carbon exchange model with emphasis on vegetation processes and surface–atmosphere coupling.
ISBA	Interaction Soil–Biosphere–Atmosphere model; includes detailed soil–vegetation–snow processes and is widely used in land–atmosphere studies.

B. Machine Learning Methods

Various machine learning techniques are applied for modelling LST and reconstructing missing pixels. These methods can be broadly categorized into two main groups: classical machine learning and deep learning. Classical machine learning includes ensemble learning models, which combine multiple decision trees for robust predictions, as well as sparse learning

and feature learning methods that focus on efficient data representation and dimensionality reduction. Deep learning models, on the other hand, leverage neural networks for complex pattern recognition. This subsection introduces the theoretical foundations of these methods.

1) Classical machine learning

Common classical machine learning methods used for gap-filling include Sparse Representation and Dictionary Learning, Random Forest, and Extreme Gradient Boosting (XGBoost). To begin, sparse representation is a method of encoding information where only a few elements in a representation vector are non-zero. It has numerous applications, including denoising, inpainting, compression, compressed sensing, and classification [25]. A dictionary matrix is used to obtain meaningful sparse representation of data. As illustrated in Figure 1, a dictionary D transforms the sparse vector x into the observed data y, following the relationship [25]:

$$y = Dx \tag{2}$$

Here, D is an overcomplete matrix, meaning it has more columns than rows ($D \in \mathbb{R}^{m \times n}$ where $m < n$) [25]. This overcompleteness provides greater flexibility in modeling, enables sparser representations, and improves robustness to noise [26]. Dictionary learning (DL) means finding the dictionary D and the sparse representations X such that the approximation $Y \approx D \cdot X$ is as good as possible. The DL problem can be naturally split into two subproblems:

- Sparse coding – Finding the optimal sparse representations X given a fixed dictionary D.
- Dictionary update – Updating the dictionary D given the current sparse representations X.

These two subproblems are solved alternately, either optimally or suboptimally, in an iterative manner. An initial dictionary is required to begin the alternating optimization process [25]. The most well-known dictionary learning algorithms are method of optimal directions (MOD) and K-SVD, both of which follow an alternating optimization approach. However, other algorithms, such as Bayesian dictionary learning, jointly infer the dictionary atoms and the sparse coefficients by performing joint optimization without strictly alternating between updating D and X. Bayesian approaches often incorporate probabilistic priors and employ techniques such as Gibbs sampling for inference, leading to more flexible and adaptive dictionary models [25].

While sparse representation and dictionary learning focus on efficiently reconstructing individual data points from a compact basis, many practical gap-filling problems also benefit from ensemble approaches that model complex relationships across multiple features. Random forest (RF) is a supervised machine learning technique that can be used for both classification and regression tasks. RF regression operates by constructing a collection of decision trees using random subsets of data and features. Each tree independently predicts a value, and the final output is obtained by averaging the predictions of all trees. The RF algorithm is regarded as efficient on large datasets, robust to noise and overfitting, and capable of handling thousands of input variables without the need for variable deletion [27]. Figure 2 shows the structure of RF regression model.

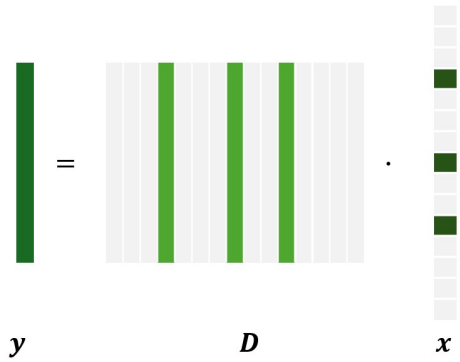

Fig. 1. Sparse representation

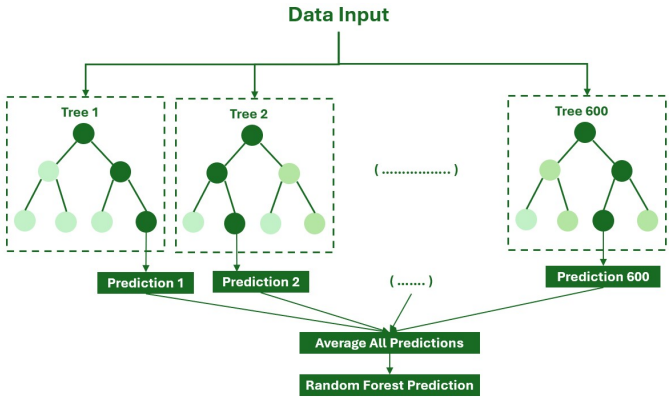

Fig. 2. Structure of random forest regression model

Building on the concept of ensemble learning, Extreme Gradient Boosting (XGBoost) takes a sequential approach rather than averaging independent trees, iteratively correcting the residual errors of prior trees. By iteratively refining these corrections, XGBoost enhances overall prediction accuracy while minimizing errors at each step [28]. Figure 3 illustrates the structure of an XGBoost model, where $f_k(X, \Theta_k)$ represents the final prediction of the k^{th} regression tree with the structure Θ_k.

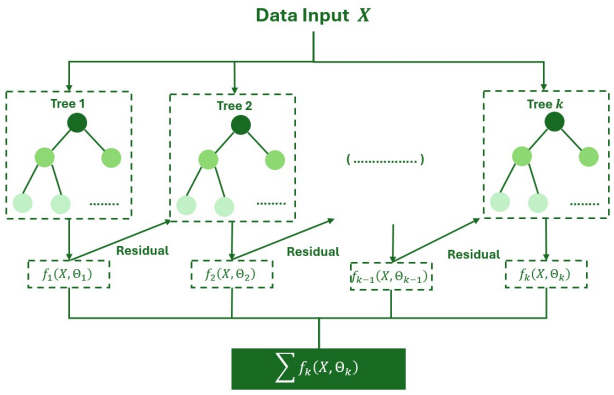

Fig. 3. The XGBoost algorithm structure

2) Deep Learning

The goal of a neural network is to learn a function that relates one or more inputs to one or more outputs with the use of training examples. Neural network architectures include feedforward networks (FFN), recurrent neural networks (RNN), convolutional neural networks (CNN), long short-term memory networks (LSTM), and generative adversarial networks (GAN). In the following, we outline the theoretical foundations of diverse deep learning methods, beginning with CNNs, a widely used and well-established architecture [29]. The standard CNN architecture alternates between convolution, pooling, and activation layers. First, the convolution layer applies filters (kernels) to the input, scanning small regions to detect spatial features such as edges, textures, and patterns. These filters slide across the input, performing element-wise multiplications and summing the results to generate feature maps that capture higher-level representations. Second, the pooling layer reduces the dimensions of these feature maps, allowing the network to retain the most important features through downsampling. Third, the activation function introduces non-linearity into the model, enabling it to learn complex patterns. Without an activation function, the network would essentially become a linear model, regardless of the number of layers, significantly limiting its capacity to model the intricate relationships present in real-world data [30]. Figure 4 illustrates the fundamental architecture of CNN. Numerous CNN architectures have been introduced, including LeNet [31], the pioneer CNN architecture, AlexNet [32], VGGNet [33], ResNet [34], GoogleLeNet [35], and U-Net [36], among others.

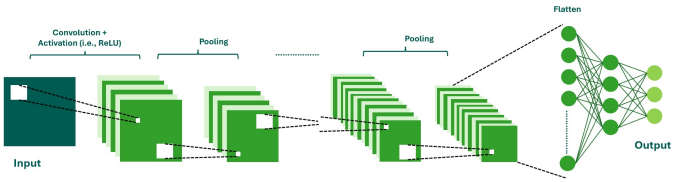

Fig. 4. CNN architecture

While CNNs are designed primarily to capture spatial structure, many LST reconstruction tasks also require modeling temporal dependencies. Figure 5 illustrates the difference between a simple FFN and RNN. RNNs incorporate a memory mechanism but struggle with long-term dependencies due to the vanishing gradient problem [37]–[39].

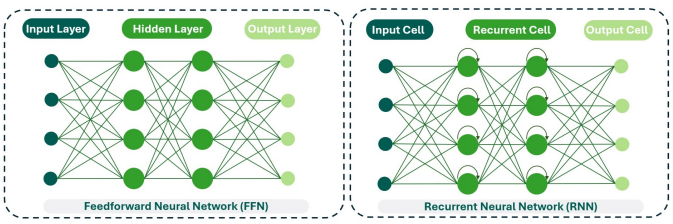

Fig. 5. Recurrent vs Feed Forward Neural Network

In an RNN, the memory mechanism is implemented through a hidden state, which is updated based on a combination of the previous hidden state and the current input, passed through an activation function (such as tanh or ReLU). LSTMs improve upon RNNs by introducing a cell state and gating mechanisms, allowing them to retain information over longer sequences and mitigate gradient-related issues [37]. An LSTM unit (or cell) maintains two states: the hidden state, which captures short-term information, and the cell state, which retains long-term information. As information propagates through deeper layers of the network, the hidden and cell states are continuously updated. The hidden state serves as the output, while the cell state evolves internally, influencing the hidden state throughout the sequence.

LSTMs utilize three gates to regulate information flow as illustrated in Figure 6. The functional purpose of the gates is as follows [39]:

1) Forget gate: determines which information from the cell state should be discarded.
2) Input gate: decides which new information will be added to the cell state.
3) Output gate: controls the output of the hidden state.

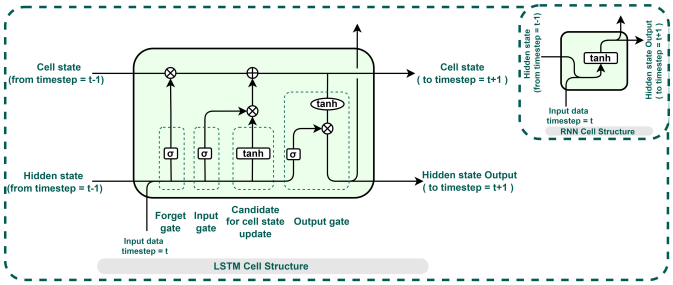

Fig. 6. LSTM architecture and gating mechanisms

Beyond sequence-based architectures, generative models constitute a complementary class of methods capable of reconstructing missing spatial information. A GAN consists of two distinct neural networks: a generator and a discriminator, which are trained in an adversarial manner [40]. The generator is designed to create realistic images, while the discriminator learns to differentiate between real-world examples and generated images. Through this competitive process, the generator continuously improves its ability to generate realistic images, while the discriminator enhances its capability to detect synthetic data, ultimately enabling the generator to produce highly realistic images. Figure 7 illustrates the basic structure of a GAN.

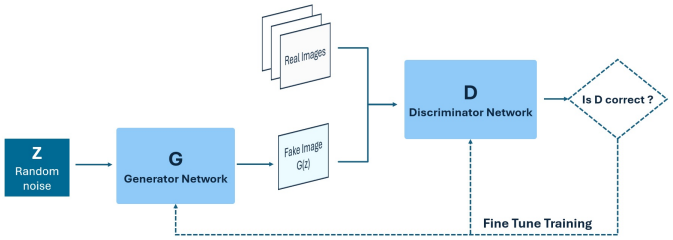

Fig. 7. Basic architecture of a GAN network

Over twelve variants of GANs have been developed, including Deep Convolutional GAN (DCGAN) [41] and Conditional

GAN (cGAN) [42]. GANs have shown superior performance in image inpainting tasks [43], making them well-suited for applications in remote sensing and environmental monitoring.

III. State-of-the-Art for Gap-Free LST Generation

To address the problem of missing or cloud-contaminated pixels in satellite imagery, numerous gap-filling strategies have been developed, ranging from spatial and temporal interpolations to integrated spatiotemporal frameworks. The latter leverage spatial context and temporal continuity, implemented either through single-sensor reconstruction or multi-source data fusion. More recently, machine learning–based methods have been widely adopted, leveraging their ability to capture complex nonlinear relationships. In addition, physics-enhanced formulations have been introduced, in which SEB constraints and physics-derived or simulated data are incorporated to guide the reconstruction process and ensure physical plausibility. Figure 8 illustrates the taxonomy of gap-filling methodologies for cloud-contaminated LST observations. These approaches are categorized into spatial, temporal, and spatiotemporal techniques, as well as emerging frameworks based on machine learning and physics-enhanced modeling. This section provides a comprehensive review of the methods reported in the literature for reconstructing missing LST data, highlighting their underlying principles, strengths, and limitations. Each method is described by outlining its specific application to LST reconstruction, with information on dataset sources, geographic scope, and temporal extent. In addition, the methods are compared to illustrate the evolution of gap-filling strategies over time, showing how more recent studies have progressively addressed the limitations identified in earlier approaches.

A. Spatial gap-filling

Spatial gap-filling approaches reconstruct missing LST values using information from spatially adjacent pixels. Common techniques include simple arithmetic means (SAM), correlation coefficient weighing (CCW), inverse distance weighting (IDW), multiple linear regression (MLR), ordinary kriging (OK), regression kriging (RK), and spline curves. IDW is largely a reflection of Waldo Tobler's first law in geography which states that "everything is related to everything else, but near things are more related than distant things" [44]. The method estimates a missing value z at a specific location x by calculating a weighted average of nearby observations. The weights assigned to these observations are inversely proportional to their distances from the location being estimated, giving greater influence to closer points [45]. Similarly, OK provides an estimate of a missing point based on the weighted average of observed neighboring points within a specific area. However, the weights in OK are calculated using the spatial structure parameters derived from a variogram; see Figure 9 [46]. A variogram quantifies spatial dependence in a dataset by analyzing the relationship between squared differences of observations and the distances separating them [46]. RK extends OK by incorporating auxiliary variables into the estimation process. It is a two-step method combining regression modeling and spatial interpolation. Initially, regression is applied to model the relationship between the target variable and auxiliary variable. The residuals from this regression are then spatially interpolated using OK [47]. For LST reconstruction, RK incorporates auxiliary data such as normalized difference vegetation index (NDVI), elevation, longitude, and latitude. Ke et al. [48] applied RK for the reconstruction of MODIS LST in Central Qinghai-Tibet Plateau. Finally, an alternative spatial reconstruction technique is based on spline curves. A spline curve is a mathematical representation used to model complex curves or surfaces, defined by a set of control points. There are two main types of splines: an interpolating spline, which passes through each control point, and an approximating spline, which stays close to the control points but doesn't necessarily pass through them. The interpolating spline is particularly useful for filling in missing data as it ensures the reconstructed surface aligns closely with known values. On the other hand, the approximating spline can be used when approximation is sufficient, providing a smoother transition between known and missing data points. Spline curves offer flexibility in handling complex datasets with varying patterns, as they allow adjustments to key parameters, including the degree of the spline function, the number and placement of the knots (points that connect polynomial pieces), and the free coefficients of the spline. A frequently used model for LST is the piecewise cubic polynomial spline. In the context of LST reconstruction, spline curves are used to estimate missing or cloudy pixels by fitting a smooth, continuous surface based on surrounding valid LST values. Spline spatial interpolation has been applied in several studies to reconstruct cloudy pixels, such as in the reconstruction of cloudy pixels in MSG-SEVIRI data during July 2010, October 2010, January 2011, and April 2011 [49].

B. Temporal gap-filling

Temporal gap-filling reconstructs missing LST values by exploiting information from nearby dates in the same pixel. This subsection outlines common temporal gap-filling techniques, including Harmonic Analysis of Time Series (HANTS) algorithm, Singular Spectrum Analysis (SSA), and Annual Temperature Cycle (ATC) modeling.

The HANTS approach, which applies harmonic analysis to time series data, was originally developed to fill gaps in NDVI maps [50]. It builds upon the Maximum Value Compositing (MVC) technique, with the key assumption that unwanted distortions (e.g., clouds, atmospheric haze) tend to appear as negative values in time-series data (e.g., NDVI, LST). The algorithm operates in two main steps: a preceding Fast Fourier Transform (FFT) analysis and a least squares curve fitting procedure. The application of HANTS in LST reconstruction demonstrates its range across different data scales. Xu et al. [51] applied HANTS to the lower-spatial resolution MODIS 8-day composite products (1km) for the year 2005 over the highly cloudy Yangtze River Delta region of China. They validated their results using simulated dataset built from high-quality pixels where missing values were

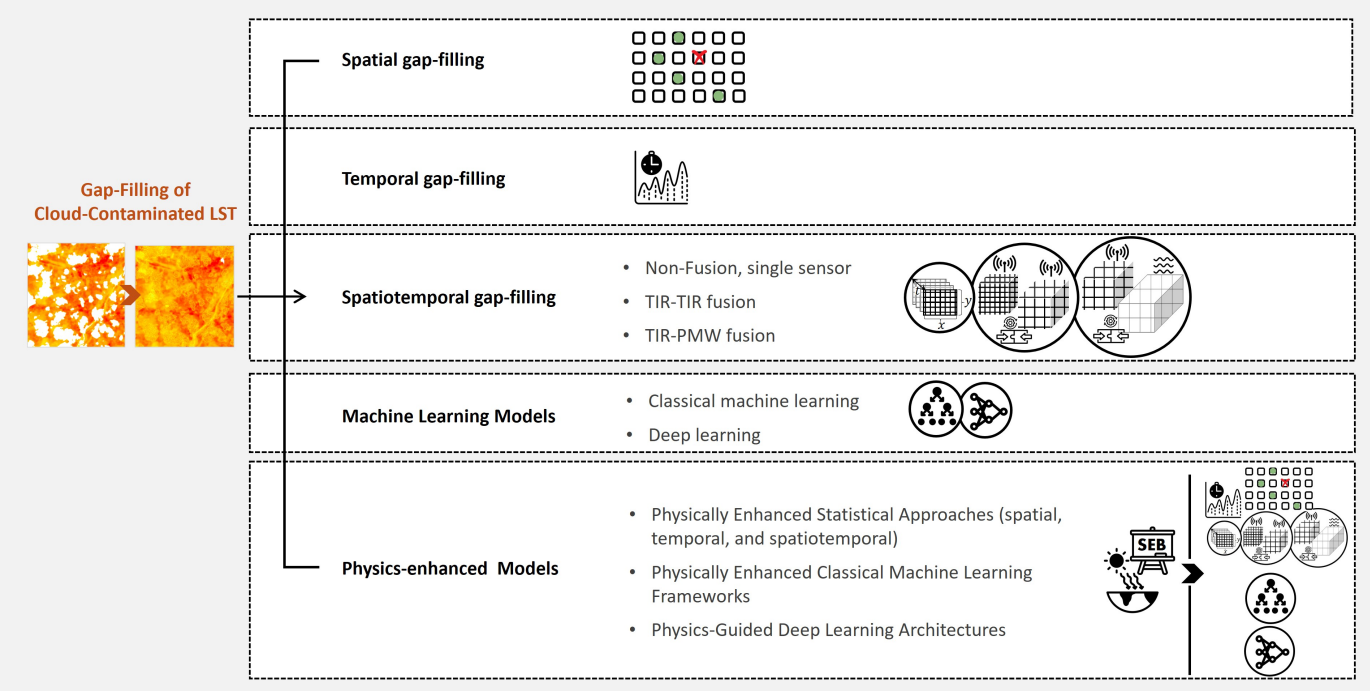

Fig. 8. Classification of gap-filling methods for cloud-contaminated LST remote sensing observations

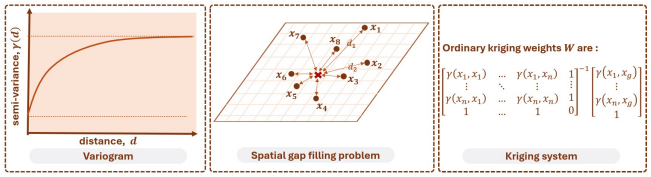

Fig. 9. Ordinary Kriging approach

artificially introduced achieving a Mean Absolute Error (MAE) of 1.51 K. Meanwhile, Aliabad et al. [52] focused on the high-spatial resolution Landsat 8 and 9 imagery (100m) over the arid Yazd-Ardakan plain in Iran for the years 2022 and 2023. Validation against simulated gaps yielded an RMSE of 3.2 K, but validation against in-situ ground measurements resulted in a significantly higher RMSE of 5.35 K. This confirms that HANTS is computationally efficient and requires minimal auxiliary data, making it a strong baseline model. However, its core limitation is the over-smoothing effect: because it relies on a small set of annual harmonics, it inevitably filters out necessary high-frequency variability, such as non-periodic weather events (e.g., short heatwaves or cold spells) and sharp localized changes that are critical for modern climate studies. More critically, the escalation of error across these three tiers is analytically significant. The error increases substantially from low-resolution simulated data (1.51 K) to high-resolution simulated data (3.2 K), confirming the temporal model's high sensitivity to increased spatial heterogeneity and noise present in finer-resolution products. The jump, from 3.2 K (simulated gaps) to 5.35 K (in-situ validation), is attributed to a combination of validation deficiencies and physical shortcomings. The RMSE discrepancy arises because simulated gap validation tests HANTS's ability to recover the ideal cloud-free LST signal. In contrast, validation against in-situ ground measurements includes errors from scale mismatch (point vs. 100m pixel) and the reality that HANTS assumes cloud-free LST, while real clouds decrease LST. This means the ground-measured temperature is often lower than the model's hypothetical reconstructed temperature.

In contrast to HANTS, SSA offers a more mathematically robust method for time series decomposition. SSA achieves a richer breakdown of the LST signal into elementary components—including trends, periodic fluctuations, and residual noise—using empirical orthogonal functions (EOFs). This approach implicitly allows for the capture of non-linear and non-periodic variations that HANTS explicitly discards. Malamiri et al. [53] applied SSA to reconstruct missing pixels over large part of Iran, Turkmenistan, and the Caspian Sea in daily MODIS LST products for the year 2015, which have a spatial resolution of approximately 1 km. The average reconstruction RMSE across the entire study region was 2.95 K. The authors compared their results to HANTS algorithm in the same region, which reported an average RMSE of 3.87 K.

Despite the analytical sophistication offered by methods like SSA, other approaches prioritize modeling the dominant, observed annual periodicity with minimal complexity, leading to the development of simple curve-fitting models. The ATC model is formulated to capture the periodic fluctuations in temperature throughout the year, reflecting the natural seasonal variations driven by Earth's orbit and axial tilt. A sine function is fitted using a least square optimization resulting in the annual cycle parameters: mean annual surface temperature (MAST), yearly amplitude of surface temperature (YAST), and a phase shift θ that accounts for the time difference

between radiative forcing and boundary conditions such as the air temperature [54]. However, the simplicity of the ATC model imposes significant limitations on its predictive accuracy. For instance, Liu et al. [55] evaluated its performance using daily MODIS LST over Mainland China, reporting an overall RMSE of 5.2 K for daytime and 3.5 K for nighttime. More critically, they highlight that ATC frequently resulted in substantial underestimation or overestimation of LSTs during short, key intervals within the annual cycle, such as between Day of Year (DOY) 90 and 150 (spring transition), or DOY 250 and 340 (autumn cooling). This demonstrates that the singular sine wave is insufficient to capture high-frequency LST variability and the complex timing of seasonal shifts. As a result, numerous adaptations of the ATC were proposed. For example, Zou at al. [56] proposed the enhanced ATC (ATCE) which additionally incorporates daily Surface Air Temperatures (SATs) to capture day-to-day LST fluctuations. It also assimilates satellite-derived NDVI to measure the LST variations caused by vegetation phenology. When tested over the Yangtze River Delta, China and compared against the ATC, the overall RMSEs of the ATCE decreased by 1.0 K for the day and 0.8 K for the night. Another adaption is propoesed by Liu et al. [55] and referred to as the hybrid ATC model (ATCH). It enhances the original ATC by incorporating multiple harmonics and a linear function of auxiliary variables influencing LST variations, including surface air temperature (SAT), NDVI, albedo, soil moisture, and relative humidity. The ATCH model has demonstrated a better performance in predicting LSTs under cloudy conditions compared to RK interpolation. These models are often integrated as a component of a more sophisticated spatiotemporal reconstruction framework discussed in Section III-C.

C. Spatiotemporal gap-filling

Spatiotemporal gap-filling techniques leverage both spatial and temporal correlations to reconstruct missing values in LST datasets. By incorporating information from neighboring pixels and adjacent time steps, these methods are particularly effective when large spatial gaps or consecutive missing dates occur. This complementary use of spatial and temporal patterns enables more robust and reliable reconstruction compared with approaches relying solely on spatial or temporal data. Within the domain of spatiotemporal reconstruction, two principal strategies have emerged, distinguished by the nature of their input data: models that operate exclusively on a single-sensor time series and those that integrate observations from multiple sensors via data fusion techniques. Figure 10 illustrates the principal categories of spatiotemporal LST gap-filling approaches, ranging from non-fusion methods to fusion-based strategies. This subsection reviews several representative spatiotemporal gap-filling models and critically evaluates their methodological foundations, performance characteristics, and practical limitations.

1) Non-Fusion Spatiotemporal Approaches

Non-fusion spatiotemporal approaches are methods that derive their solution purely from the inherent statistical relationships found within a single LST data record. For example, Siabi et al. [57] introduced the Differential Dynamic Search Distance Algorithm (DDSDA) as an effective and computationally efficient method for filling gaps in MODIS 8-day LST products from 2000 to 2018 across a 1,648,195 km^2 region of Iran. DDSDA combines temporal information with spatial cues from neighboring pixels and operates on a set of seasonal images, that is, images acquired on the same month and day as the target scene but from different years. Using a validation set of 400 images with artificially generated gaps ranging from 4% to 96%, the method achieved a mean MAE of 0.66 K, with an MAE of 2.03 k reported specifically for large gaps. Following an analogous methodology, Sun et al. [58] proposed the Remotely Sensed DAily land Surface Temperature reconstruction (RSDAST) model, which utilizes spatial and temporal neighboring pixel interpolation for LST gap-filling. The method employs a weighted function based on the distance to the gap pixel and the LST difference from a nearby clear-sky date to enhance reconstruction accuracy. Interpolation is performed using valid data in a 9×9 pixel window from the nearest 8 days. The model is applied to MODIS LST data in two study areas located in Northwest China: a plain region with little heterogeneity and a mountainous region with complex terrain and strong heterogeneity. Initial validation using artificially masked pixels on three dates between 2000 and 2002 yielded RMSE values of 0.92–1.16 K for the plain region (gap size 84%) and 1.42–2.24 K for the mountainous region (gap size 58%). The model was subsequently applied to reconstruct cloud-contaminated pixels on two dates in 2014. A third framework by Zhang et al. [59] follows a similar approach to reconstruct missing daily MODIS LST pixels, generating a global seamless 1 km dataset for 2003–2020. The method proceeds in two steps. First, initial gaps in the target observation are filled using LST measurements from the three other same-day time points, merged via linear regression or a shift-based adjustment, depending on the percent of valid data. Second, the temporal trend of each pixel is estimated by fitting a smoothing spline to capture the seasonal cycle, and daily residuals are interpolated spatiotemporally using the Correlation Weighting (ICW) technique. Missing values are then reconstructed by summing the trend and interpolated residuals. Validation was performed on artificially generated gaps using data from 2005, 2010, and 2015, across 15 randomly selected MODIS tiles worldwide, yielding RMSE values of 1.88 K for daytime and 1.33 K for nighttime.

Moving beyond standard spatiotemporal interpolation techniques, which typically assume that missing values can be approximated by the average or weighted average of surrounding observations, more sophisticated reconstruction frameworks have been proposed. For example, Gerber et al. [60] developed the GapFill R package for spatiotemporal reconstruction of remote sensing data, initially validating it using MODIS NDVI. Subsequent studies [61], [62] extended its application to LST, although reconstruction errors for LST are generally higher than for NDVI. This difference is primarily attributed to the nature of the variables: NDVI is a unitless index constrained between 0 and 1, whereas LST spans a much wider dynamic range in Kelvin. The core of the GapFill algorithm is a quantile regression process that assumes data subsets within a

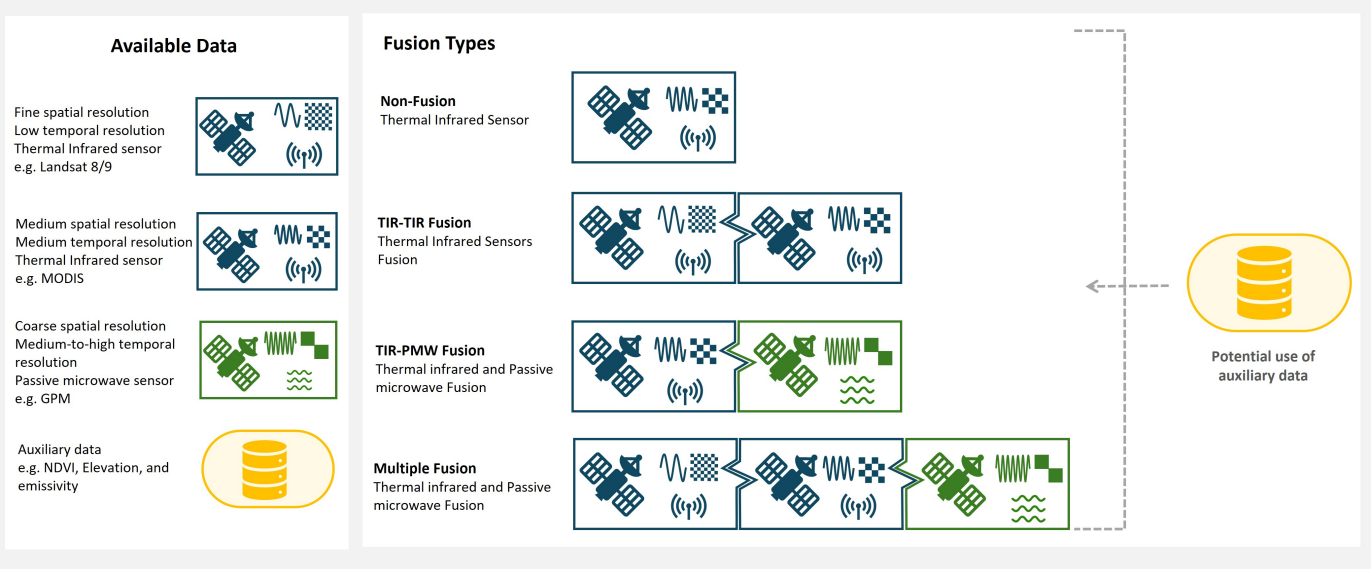

Fig. 10. Main categories of spatiotemporal LST gap-filling approaches

spatiotemporal window share similar spatial patterns to the target image, but are merely shifted in time. Rather than averaging neighboring observation, GapFill computes scores to measure the similarity of these neighboring subsets to the target area, ranks them based on these scores, and constructs a quantile regression model using the observed LST as the dependent variable and the subset ranks as the explanatory variable to predict the missing pixel. Li et al. [62] improved the performance and efficiency of GapFill by introducing a three-step hybrid framework in which the four daily MODIS observations (Terra day/night and Aqua day/night) are first merged using linear regression and temporal shifting, substantially reducing gap size and frequency before applying the computationally intensive GapFill algorithm. Any remaining small gaps are subsequently filled using simple temporal interpolation. Applied to reconstruct a seamless 1 km daily LST dataset over urban and surrounding areas across the conterminous United States for 2010, this hybrid approach reduced RMSE from 3.95 K (standalone GapFill) to 3.5 K. More importantly, it improved computational efficiency: whereas standalone GapFill required an average of 22 iterations to fill large gaps, the hybrid framework reduced this to four iterations by shrinking gaps beforehand, achieving a 4.5-fold reduction in processing time while maintaining complete spatial coverage. In contrast, Militino et al. [61] proposed the Interpolation of the Mean Anomalies (IMA) method, which retains GapFill's definition of a spatiotemporal neighborhood. Like GapFill, IMA defines the neighborhood of a target image to include not only the preceding and subsequent images from the same year but also images from the same dates in previous and subsequent years. However, while GapFill's approach relies on quantile regression and the ranking of pixel values, IMA's approach computes a mean target image from the neighborhood. It then calculates anomalies (residuals) by subtracting this mean from the observed data, filters extreme values, and interpolates the anomalies using spatial spline interpolation, then adds the reconstructed anomalies back to the mean image to generate the final estimates. Validated using MODIS LST data over Navarre, Spain (2011–2013), IMA achieved RMSEs of 1.41–2.48 K for daytime and 1.22–1.99 K for nighttime conditions, outperforming GapFill (1.8–2.81 K daytime; 1.46–2.2 K nighttime). IMA also demonstrated an improved computational efficiency, filling gaps in approximately 4 seconds compared to 1.5 hours for GapFill, an improvement of several orders of magnitude attributed to solving a system of linear equations rather than iteratively ranking pixels. Overall, Li et al. [62] enhanced robustness by reducing gap size prior to reconstruction, preventing excessive iterations, while Militino et al. [61] addressed fundamental limitations of GapFill itself by eliminating pixel ranking, which can fail when large gaps produce ties, thereby ensuring stability regardless of gap size.

Another unique approach combines Discrete Cosine Transforms (DCT) with a Penalized Least Squares (PLS) regression approach. The resulting DCT-PLS method is a multi-dimensional, robust smoothing algorithm originally developed by Garcia [63]. This method operates by utilizing data available in both space and time to iteratively update missing values, aiming to find an optimal balance between fidelity (staying true to the original valid data points) and smoothness (reducing roughness or noise). The process is controlled by a smoothing parameter: lower values retain high-frequency components, preserving sharp spatial details and extremes, whereas higher values produce smoother fields. Recent studies have applied DCT-PLS to reconstruct MODIS LST data at continental and global scales, focusing on optimizing the smoothing parameter for different temporal resolutions. Pham et al. [64] applied a 3D DCT-PLS to fill gaps in 9 years of daily MODIS LST data over Australia and Liu et al. [65] applied the method to monthly MODIS daytime LST data (2001–2017) across Africa, Southeast Asia, and South America. The key difference between these applications lies in the parameter

optimization strategy suitable for their respective temporal resolutions: Pham et al. manually determined that optimal smoothing differs by time of day, recommending smoothing parameter $\leq 10^{-6}$ for daytime and $\leq 10^{-4}$ for nighttime to avoid over-smoothing high-frequency daily variations. In contrast, Liu et al. [65] utilized the Generalized Cross-Validation (GCV) criterion to automatically select the optimal smoothing parameter during the iteration process to balance bias and variance for monthly data. The GCV criterion calculates a specific score based on the prediction error (how far the estimate is from the data) normalized by the roughness of the smoothing matrix. The algorithm searches for the smoothing parameter value that minimizes this GCV score, thereby mathematically identifying the optimal parameter where the trade-off between error and variance (noise) is optimized Regarding accuracy, Pham et al. achieved an RMSE between 2.0 K and 3.9 K when validated against ground-based measurements, while Liu et al. reported an average RMSE of 0.91 K using synthetic gap validation, demonstrating high fidelity to spatial patterns even over large gaps.

Another method is the Data Interpolating Empirical Orthogonal Functions algorithm (DINEOF) applied by Zhou et al. [66] to reconstruct missing pixels in daily MODIS LST on the region around Ali on the Tibetan Plateau, an area of about 40,000 km^2, characterized by mountains and valleys with altitudes ranging from 3870 to 6460m. Validtion with artifically masked pixels achieved an RMSE of 4.57 K during daytime and 2.30 K at night. DINEOF is an iterative, unsupervised method that reconstructs missing values based on the Empirical Orthogonal Function (EOF) and without requiring additional external data [67]. EOF analysis is often used to identify dominant spatial modes (i.e., patterns) of variability and how they change over time [68] in geophysical and climate datasets, such as sea surface temperatures and atmospheric pressure fields [69].

Collectively, these methods illustrate a methodological trade-off that exposes the limits of pure statistical approaches. They all rely purely on the internal temporal and spatial structure of LST data and require no auxiliary information. DDSDA and RSDAST rely on localized spatial–temporal neighborhoods and seasonal analogs, whereas DINEOF exploits large-scale spatial–temporal covariance patterns through an EOF decomposition. Their performance varies with landscape heterogeneity and the structure of missing data.

This has motivated the development of more advanced spatiotemporal approaches that incorporate auxiliary information—such as vegetation indices, elevation, or land cover to better constrain the reconstruction process. Spatiotemporal methods that incorporate external predictors aim to overcome the limitations of purely internal statistical reconstructions by integrating additional environmental information. One such approach proposed by Metz et al. [70] to produce gap-free 1 km MODIS LST data over Central Europe, generating four daily records from Terra and Aqua overpasses (approx. 01:30, 10:30, 13:30, and 22:30 local solar time) for the period 2003–2016. The method first applies temporal interpolation using Local Weighted Regression (LWR) to preserve short-term variability and extreme events, and subsequently fills small temporal gaps using valid observations from the same pixel. Remaining gaps are then filled using Thin Plate Spline (TPS) interpolation with neighboring pixels and auxiliary predictors (elevation and emissivity), employing an adaptive window based on the nearest 150 valid points to minimize artifacts. Crucially, the inclusion of emissivity as a predictor allowed the method to preserve high-frequency spatial details, such as the thermal distinction between urban areas, water bodies, and vegetation; this was visually confirmed over a region covering Switzerland, France, and Germany, where urban areas and water bodies were correctly depicted as warmer than their surroundings in winter. The study also confirmed the method successfully captured extreme climatological anomalies, specifically reproducing the high intensity and spatial extent of the August 2003 European heatwave. The robustness of the method was assessed by introducing artificial gaps of varying sizes (9–1,425 pixels) into a cloud-free Aqua daytime overpass from 23 June 2016; reconstruction performance was quantified using mean bias (difference), with errors increasing from -1.2 K for a 9-pixel gap to -2.7 K for a 1425-pixel gap. A second framework by Tan et al. [71] reconstructs the LST values affected by cloud cover in daily MODIS observations from 2013–2018 over the Heihe River Basin (HRB) in arid Northwest China, with the aim of generating LST all-weather (actual cloudy skies) LST. The method follows a two-step approach: in the first step, the theoretical clear-sky LST for cloudy pixels is reconstructed by identifying thermally similar pixels based on the combined influence of five environmental factors: NDVI, theoretical clear-sky radiation, elevation, slope, and aspect, and applying a linear transfer function. In the second step, a bias correction is performed on the theoretical clear-sky LST to derive the final cloudy-sky LST. This correction statistically estimates the cloud effect temperature term by comparing theoretical clear-sky LST with in-situ LST under cloudy conditions for different land-cover types, and applies variance scaling to reduce residual systematic biases. Validation results reported RMSE values ranging from 3.40 K to 5.66 K for daytime and 2.57 K to 3.47 K for nighttime. While incorporating geophysical predictors should theoretically yield lower error, the two-step bias correction approach of Tan et al. [71] resulted in higher RMSE values, ranging from 3.40 K to 5.66 K for daytime reconstruction. Another approach leveraging the ATC model as a temporally consistent statistical baseline, Zhu et al. [72] proposed the ATC-IDW framework to generate gap-free clear-sky Landsat 8 LST. In this framework, the final reconstructed LST is calculated as the sum of a reference temperature derived from the ATC model and a residual term that accounts for fine-scale deviations. Using Landsat data from 2013 to 2020, the ATC model was fitted to provide a baseline temperature. IDW is then applied to refine the spatial component and estimate the residual term, the algorithm applies a fixed-radius window around the cloudy pixel to identify spatially similar neighbors. These neighboring pixels are assigned weights based on their similarity to the target pixel in terms of Euclidean distance, NDVI, and their ATC-modeled temperatures. The final LST residual is then computed using these weights. When tested on images with cloud cover ranging from approximately 49% to

66%, the method achieved RMSE values between 0.9 and 2.5 K for artificial gaps. However, when validated against true in-situ ground measurements, the RMSE ranged from 2.5 to 3.9 K, highlighting the persistent challenge of reconciling satellite-scale temporal models with point-based surface observations.

The performance of these methods incorporating external predictors reveals a clear trade-off: simply adding auxiliary data does not guarantee lower overall errors, as model complexity and the specific correction strategy often play a more decisive role. It is observed that real-world validation continues to expose residual uncertainties that artificially masked gap tests fail to capture. Furthermore, the reliance on external variables introduces new analytical weaknesses: the two-step reconstruction by Tan et al. [71] is computationally complex and depends heavily on the availability of localized in-situ data for its crucial bias correction step, severely limiting the general applicability and global transferability of the methodology. Overall, this does not imply that incorporating auxiliary data is inherently disadvantageous; rather, it highlights that environmental information needs to be better leveraged.

The core algorithmic structures, auxiliary data requirements, and validation results of the spatiotemporal LST reconstruction methods discussed in this section are synthesized and compared in Table III.

2) Spatiotemporal Data Fusion (Fusion Methods)

Fusion methods integrate observations from multiple satellite sensors to leverage complementary strengths. They can be broadly grouped into two categories: TIR–TIR fusion and TIR–PMW fusion.

TIR–TIR approaches combine thermal infrared observations from sensors with complementary spatial and temporal characteristics—for example, pairing the frequent revisit capability of MODIS with the finer spatial resolution of Landsat—to generate LST products with enhanced spatial detail and increased revisit frequency. The Spatial and Temporal Adaptive Reflectance Fusion Model (STARFM), an early model originally developed for surface reflectance [73], provided the conceptual foundation for subsequent extensions to LST fusion. STARFM predicts fine-resolution pixel values by blending information from spectrally similar neighboring pixels within a moving window, with weights determined by spectral similarity, temporal proximity, and spatial distance. However, its applicability is constrained by the assumption of unchanged land cover between reference and prediction dates, making it less effective in areas experiencing abrupt changes such as flooding or urban expansion, and its performance degrades in highly heterogeneous landscapes.

Its successor, the enhanced STARFM (ESTARFM) [74], improves performance in heterogeneous areas by using a linear spectral mixing model that requires two pairs of fine- and coarse-resolution images. Another extension, the Spatiotemporal Adaptive Data Fusion Algorithm for Temperature mapping (SADFAT) [75], is a specialized adaptation of STARFM designed explicitly for LST fusion. SADFAT enhances the STARFM framework by incorporating a nonlinear ATC model to capture annual LST variations and by employing Linear Spectral Mixture Analysis (LSMA) to account for temporal changes in radiance during the fusion process. When tested in Los Angeles County, California, SADFAT achieved an MAE ranging from 1.3 K to 2.0 K. While both ESTARFM and SADFAT aim to improve performance in heterogeneous regions, they do so via different strategies: ESTARFM relies on a linear spectral mixture formulation, whereas SADFAT leverages a nonlinear ATC-based model better suited to the intrinsic nonlinearities of LST dynamics. Consequently, SADFAT is generally expected to provide higher accuracy than ESTARFM for LST fusion, as it is specifically tailored to the nonlinear characteristics of LST, while ESTARFM remains constrained by the linear reflectance-based assumptions.

A key challenge in applying ESTARFM, or SADFAT directly to LST fusion is that LST observations from different sensors are often not radiometrically comparable due to differences in retrieval algorithms, viewing geometry, and acquisition times, which introduce systematic biases. To address these issues, the unbiased ESTARFM (ubESTARFM) variant [76] was developed, incorporating a local correction strategy that compensates for sensor-dependent systematic biases in fine-resolution LST by referencing the mean value of corresponding coarse-resolution LST pixels. In a continental-scale evaluation across Australia (2013–2021), Yu et al. [76] demonstrated that ubESTARFM substantially outperforms ESTARFM, achieving an overall bias of 2.55 K and an unbiased RMSE (ubRMSE) of 2.57 K against in-situ LST, compared to ESTARFM's bias of 4.73 K and ubRMSE of 3.80 K, demonstrating superior robustness in bias control and uncertainty reduction. The ubESTARFM framework has also shown potential for fusion involving geostationary sensors such as Himawari-8.

While two-sensor fusion models such as STARFM, ESTARFM, and their LST-oriented variants have shown promise, they often struggle when the spatial resolution gap between sensors becomes too large—such as when fusing fine-resolution Landsat data with coarse geostationary observations (e.g., GOES or SEVIRI). The Spatio-Temporal Integrated Temperature Fusion Model (STITFM) [77] was introduced to address this limitation by providing a unified framework capable of fusing LST data from an arbitrary number of sensors spanning fine, moderate, and coarse spatial scales. By incorporating an intermediate-resolution dataset (e.g., MODIS), STITFM effectively narrows the large spatial discrepancy, stabilizes local fusion variables, and reduces inter-sensor biases. In practice, this multi-scale strategy has proven advantageous: STITFM demonstrated that predictions obtained from three sensors consistently outperform those derived from only two. For example, in the southwestern United States, fusing Landsat, MODIS, and GOES data reduced the RMSE from 4.06 K (two sensors) to 1.40 K, and in Evora, Portugal, combining Landsat, MODIS, and SEVIRI yielded an RMSE of 2.2 K, compared to 3.3 K for the two-sensor fusion, underscoring the substantial benefits of incorporating an intermediate resolution sensor to bridge large spatial gaps. Similarly, the integrated spatiotemporal fusion algorithm (ISFAT) [78] applies the three-resolution strategy. ISFAT is a two-stage model designed to generate fine-scale LST data, integrating elements from both SADFAT and STITFM. The first stage focuses on fine-scale prediction on the prediction date, improving SADFAT by using

TABLE III
SYNTHESIS OF REPRESENTATIVE NON-FUSION SPATIOTEMPORAL METHODS FOR LST RECONSTRUCTION UNDER CLOUD COVER.

Method	Core Algorithm	Aux. Variables	Spatial Scope	Validation Type	RMSE (K)	Key Assumption	Major Limitation
DDSDA [57]	Differential dynamic search distance	None	Regional (Iran)	Artificial masking	0.66 (avg); 2.03 (large gaps)	Seasonal recurrence across years	Sensitive to land-cover change and anomalous climate variability
RSDAST [58]	Weighted spatial–temporal interpolation	None	Regional (NW China; plains vs. mountains)	Artificial masking	0.92–1.16 (plains); 1.42–2.24 (mountains)	Local spatial similarity within 9×9 window	Performance degrades in heterogeneous terrain
ICW Framework [59]	Multi-pass merging + spline interpolation	None	Global (15 MODIS tiles)	Artificial masking	1.88 (Day); 1.33 (Night)	Stable seasonal trends and residual smoothness	Residual smoothing may dampen thermal extremes
GapFill [60]	Quantile regression + similarity ranking	None	Continental (US; Spain)	Artificial masking	1.8–3.95	Similar spatiotemporal subsets exist for ranking	High computational demand; sensitive to subset definition
Hybrid GapFill [62]	Linear regression + GapFill	None	Continental (US)	Artificial masking	3.5	Pre-reduction of gap size improves efficiency	Accuracy remains terrain-dependent
IMA [61]	Mean anomaly + spline interpolation	None	Regional (Spain)	Artificial masking	1.22–2.48 (Day); 1.22–1.99 (Night)	Stable anomaly structure over time	Limited performance under prolonged cloud cover
DCT-PLS [64], [65]	Discrete Cosine Transform + Penalized Least Squares	None	Global (multi-continental validation)	Synthetic + In-situ	0.91 (synthetic); 3.9 (in-situ)	Dominant low-frequency spatiotemporal modes capture variability	Potential oversmoothing of localized extremes
DINEOF [66]	Empirical Orthogonal Function decomposition	None	Regional (Tibetan Plateau)	Artificial masking	4.57 (Day); 2.30 (Night)	Dominant EOF modes represent variability	High daytime error; large-scale bias in complex terrain
LWR+TPS [70]	Local weighted regression + thin-plate splines	Elevation, Emissivity	Regional	Artificial masking	1.2–2.7	Terrain and emissivity explain sub-pixel thermal variability	Window size strongly affects artifact suppression
Tan et al. [71]	Linear transfer + bias correction	NDVI, Elevation, Aspect, Slope	Regional	In-situ dependent	2.57–5.66	Linear correction adequate under stable terrain–vegetation relations	Heavily dependent on localized ground observations
ATC-IDW [72]	ATC baseline + inverse distance weighting	NDVI, ATC model parameters	Regional	Artificial masking	0.9–3.9	Diurnal cycle provides stable reconstruction baseline	Scale mismatch between satellite pixels and point observations

a masked weight variable to integrate partly clouded inputs and then adjusting the residuals across the study area using a thin-plate spline (TPS), a smooth interpolation technique that mimics the bending of a thin metal sheet through given points. The second stage performs diurnal LST prediction by jointly integrating fine-, medium-, and coarse-resolution LST data, following the multi-resolution concept established by STITFM to mitigate large scale gaps. In an empirical application predicting fine LST over Hong Kong on February 18, 2020, ISFAT achieved an RMSE of 3.33 K, outperforming SADFAT (3.52 K) and STITFM (4.01 K) under the same experimental conditions. This improvement is attributable to the combined use of fine-resolution (Landsat-8), medium-resolution (Sentinel-3), and coarse-resolution (Himawari-8) LST data, which enables the model to effectively leverage complementary spatial and temporal strengths across sensors.

Another early fusion technique is the Multisensor Multiresolution Technique (MMT) [79]. It was developed to

combine images acquired at different times and resolutions by disaggregating coarse-resolution pixels into finer-resolution components (unmixing). In satellite imagery, a single coarse pixel often contains signals from multiple land-cover types (e.g., vegetation, soil, and urban surfaces). MMT estimates the contribution of each class to the coarse pixel, guided by a high-resolution classification map, and then assigns these estimated signals to the corresponding high-resolution pixels, effectively breaking down mixed pixels into finer spatial detail. The method includes physics-constrained and unconstrained variants. Developed subsequently, the Flexible Spatiotemporal DAta Fusion (FSDAF) method [80], integrates core ideas from MMT, spatial interpolation, and weighted function-based models (like STARFM) into a single unified framework. The core methodology of FSDAF involves six main, consecutive steps. FSDAF begins by classifying the fine-resolution image and globally solving a system of linear mixture equations based on class fractions to estimate the temporal change for each class, producing an initial temporal prediction and calculating residuals at the coarse pixel level. It then generates a spatial prediction using Thin Plate Spline (TPS) interpolation to guide the distribution of these residuals to fine pixels, and integrates neighborhood information via weighted averaging to produce the final robust image, capable of capturing both gradual and abrupt land cover change. The Comprehensive Flexible Spatiotemporal DAta Fusion (CFSDAF) method [81] is an enhanced version of FSDAF designed for urban, heterogeneous environments. CFSDAF modifies FSDAF by employing IDW interpolation instead of TPS interpolation to significantly improve computational efficiency. It also introduces visible and near-infrared images to perform soft classification, considering mixed fine-resolution pixels, which helps reserve spatial continuity and details. When applied to MODIS–Landsat fusion in the urban areas of Beijing and Shenzhen, China, CFSDAF consistently outperformed STARFM and FSDAF in both quantitative metrics and visual inspection. In addition, Li et al. [82] conducted a unified comparative assessment of four popular spatiotemporal fusion algorithmss—STARFM, unconstrained MMT, FSDAF, and STITFM. The evaluation employed LST data from three spatial resolutions: ASTER LST (fine, 100 m), MODIS LST (medium, 1 km), and a simulated geostationary satellite LST product (coarse, created by aggregating MODIS to 5 km). For the spatiotemporal fusion models that were originally designed as two-source algorithms (STARFM, the unconstrained MMT, and FSDAF), a two-step sequential fusion strategy was required to integrate the three satellite LST products in this comparative assessment. In Step 1, an intermediate LST image was generated by fusing the medium-resolution with the coarse-resolution simulated geostationary LST (5 km). In Step 2, the final fine-resolution LST prediction was produced by fusing the original fine-resolution ASTER LST with the intermediate MODIS-like LST generated in Step 1. Their results showed that FSDAF achieved the best overall performance, with the lowest RMSE and highest correlation coefficients. However, the comparison was limited in both spatial and temporal scope, as it was performed over a single 40 km × 40 km area in the southwestern U.S. and relied on the ASTER LST product from a single date (September 14, 2008). Furthermore, these approaches fail to address systematic biases that occur when differences between sensors are assumed to be constant.

Building on the evolution of spatiotemporal fusion methods, the Long Time-series Spatiotemporal Fusion Model (LOTSFM) [83] is a robust, recent model specifically designed for LST data fusion, aiming to generate daily LST products at 30 m spatial resolution by blending Landsat and MODIS data. The model is composed of four key components: Long Time-series Regression Model Fitting (using 79 pairs of Landsat and MODIS images from 2013 to 2022), Sensor Difference Term Estimation, Spatial Filtering, and Missing Pixel Filling. By explicitly accounting for the sensor difference—a crucial improvement over older models such as STARFM and FSDAF, which treat this term as a constant—LOTSFM achieves both stable accuracy and computational efficiency. Cross-validation results across heterogeneous urban regions (Beijing, Shanghai, and Guangzhou) demonstrated low RMSE values, ranging from 1.60 K to 2.17 K, highlighting its suitability for urban thermal environment studies. Compared to other models, LOTSFM provides more reliable and stable LST predictions under extreme temperature scenarios. However, its strength is primarily in urban regions with relatively stable land surface features, and its performance can be reduced in highly dynamic agricultural landscapes compared to other models.

Unlike previous fusion methods that focus on spatiotemporal downscaling, where a medium-resolution image (e.g., MODIS) is sharpened using a finer-resolution image (e.g., Landsat) to produce a fine-resolution product, Yao et al. [84] proposed a fusion approach aimed at image restoration through the fusion of similar-resolution products. Their method operates on a gapped image (e.g., a cloud-contaminated MODIS image) and employs a same-day partner image with comparable spatial resolution (e.g., VIIRS) to reconstruct missing regions rather than enhance spatial detail. Consequently, the method represents a conceptual improvement over single-product reconstruction approaches (such as RSDAST and IMA), rather than an evolution of spatiotemporal downscaling fusion models like STARFM or ubESTARFM. The algorithm follows five steps: removing outliers, defining a subset of 11 reference images (including 3 from other sensors on the same day and 8 from the same sensor on adjacent days), determining spatial windows, predicting the target pixel using a weighted function (based on Distance, Similarity, and Standard Deviation indices), and temporally filling any remaining gaps. Performance was evaluated using daily LST data from 2018 over two climatically distinct regions in China—the Beijing–Tianjin–Hebei region and the Pearl River Delta—by introducing artificial gaps and computing MAE. The results showed that the achieved precision is comparable to the inherent quality of the original satellite products (generally ¡1 K), with MAEs of 0.845 K (daytime) and 0.584 K (nighttime) for small gaps (20 × 20 km), and 1.031 K (daytime) and 0.805 k (nighttime) for large gaps (150 × 150 km).

The evolution of TIR–TIR fusion frameworks transitioning from early reflectance-based models to modern multi-sensor restoration and bias corrected downscaling systems is synthe-

sized in Table IV. This comparison details the core algorithmic strategies, geographic study regions, and performance metrics across diverse heterogeneous landscapes.

Having reviewed TIR–TIR fusion methods, which combine thermal infrared data from multiple sensors to improve spatial and temporal coverage, it is also important to consider TIR–PMW fusion approaches. This category directly addresses the core sensor trade-off described in Section I: while TIR provides fine spatial resolution, it is limited by cloud contamination, whereas PMW offers all-weather capability at coarse resolution. However, a significant technical challenge for integrating PMW- and TIR-based LST is the large scale gap presents (e.g., 25 km PMW vs. 1 km TIR). In addition, PMW LST products typically have lower accuracy, often resulting in fused products with step discontinuities, excessive smoothness, pronounced grid effects, or spatial streaking [85].

Several models have been developed to leverage PMW data to fill gaps and generate gapless all-weather LST. Early efforts, such as, Duan et al. [86] reconstructed cloudy pixels by downscaling microwave temperatures using elevation-based lapse rates to match the MODIS grid. Remaining orbital gaps are filled via temporal linear interpolation from adjacent days or, if unavailable, spatial IDW interpolation. This study validated its all-weather LST against in-situ measurements from four sites in the arid Heihe River Basin of northwest China. RMSE of the reconstructed data varied between 3.5 K and 4.4 K. However, a critical limitation of Duan's deterministic merging approach is the creation of artificial boundary lines and grid effects. Because the coarse AMSR-E pixels are downscaled and inserted directly into the gaps, the resulting map can show visible seams between the filled areas and the original clear-sky MODIS data.

Probabilistic methods provide seamless blending and are proposed to eliminate the undesired grid effects. The Bayesian Maximum Entropy (BME) method is a probabilistic spatiotemporal approach that integrates multisource data while accounting for differences in accuracy, producing optimal estimates even in regions with missing observations. The method primarily utilises Gaussian probability density functions (PDFs) to represent the uncertainty of the coarser microwave data, treating it as a distribution defined by a mean and variance rather than a fixed value. This specific probabilistic information is then fused with general knowledge, represented by a covariance model derived from MODIS data that describes the region's spatiotemporal temperature correlations. This fusion of information generates a posterior probability distribution for every specific location, from which the most optimal temperature estimate is finally derived. Kou et al. [87] applied the BME method to reconstruct LST over the central Tibetan Plateau (specifically around Naqu City) by blending MODIS and AMSR-E data. Validation against calibrated 0–5 cm soil temperature measurements showed RMSEs of 2.31–4.53 K. However, their study focused exclusively on night-time LST (1:30 A.M. local time). The authors intentionally avoided daytime data to minimise the uncertainties caused by sunshine warming and solar radiation effects on the validation process. Xu et al. [88] expanded on this work by testing BME under more challenging conditions, including rugged terrain, daytime, and heterogeneous land cover, over both the Tibetan Plateau and the Heihe River Basin. In validation studies, BME showed RMSE of less than 3.54 K during the nighttime and 4.89 K during the daytime over relatively flat terrain (Tibetan Platea). In rugged terrain (Heihe River Basin), errors were higher, ranging from 4.2 to 8.29 K during the daytime. While effective at gap-filling, BME results are excessively smooth or exhibit step discontinuities in regions where high-quality TIR data are largely missing [89]. Recognizing these limitations, a more advanced fusion framework based on Cumulative Distribution Function (CDF) matching and Multiresolution Kalman Filtering (MKF) was developed by Xu et al. [89]. The new approach first downscales PMW LST using a geographically weighted regression (GWR) model. The downscaled PMW LST is then adjusted via CDF matching to align its distribution with MODIS LST, generating an all-weather LST product. The accuracy of the resulting data is further improved by applying MKF to fuse the adjusted PMW LST with MODIS LST, producing a high-quality fused LST dataset. The method was applied over the Chinese landmass to generate spatially complete, all-weather LST from 2002 to 2019 by fusing AMSR2 PMW LST, with the TIR based LST MODIS. Two geographically and ecologically distinct regions were selected for validation: the Tibetan Plateau and the Heihe River Basin. In the HRB, the RMSEs was 3.23 K/3.00 K (daytime/nighttime), respectively. In the TP, the corresponding RMSEs was 3.82 K/3.31 K.

While the aforementioned models focus on reconstructing missing values directly, Dowling et al. [90] introduced a conceptual shift by utilizing PMW data as a calibration tool rather than a primary gap-filler. They implemented a two-step fusion framework to generate gap-free, all-weather LST over Kenya. In the first step, missing MODIS LST pixels are estimated using a multivariate linear regression relating LST to NDVI, elevation (DEM), and LST from adjacent days. In the second step, these preliminary estimates are calibrated using coarse AMSR-2 passive microwave observations to quantify and subtract the cloud shadowing bias, thereby correcting the temperatures for the actual cooling effect of cloud cover that the statistical model alone cannot capture. Validations against both in-situ measurements and SEVIRI satellite data demonstrated that the RMSE ranges from 2.6 K to 3.6 K during the daytime. The proposed method treats PMW as a bias calibrator rather than a gap filler. However, a primary methodological limitation is that the method calculates the cloud shadowing bias at the coarse 25 km resolution of the AMSR-2 sensor and applies this single value uniformly to all 1 km MODIS pixels within that grid. Additionally, the authors explicitly state that their method is unsuitable for use in desert regions or areas covered by snow and ice.

Traditional fusion models often process data pixel-by-pixel which is computationally slow for global datasets. To address the computational bottlenecks, Meng et al. [91] introduced the Global Spatiotemporal Fusion Model (GLOSTFM) for fusing PMW-based LST from MWRI with TIR-based LST from MERSI. Unlike probabilistic approaches such as BME [87], [88] or elevation-based downscaling methods [86], GLOSTFM employs a computer-vision strategy based on image pyramids

TABLE IV
SYNTHESIS OF REPRESENTATIVE TIR–TIR SPATIOTEMPORAL FUSION METHODS.

Method	Core Strategy	Study Region	RMSE/MAE	Major Limitation
STARFM [73]	Spectral similarity	Heterogeneous landscapes	N/A	Fails with abrupt land-cover changes.
SADFAT [75]	Nonlinear ATC + LSMA	Los Angeles, USA	1.3–2.0 K (MAE)	Computationally complex ATC modeling.
ubESTARFM [76]	Mean-based bias correction	Australia (Continental)	2.57 K	Requires sensor-specific radiometric matching.
STITFM [77]	Multi-scale (3-sensor)	SW USA; Portugal	1.4–2.2 K	Relies on availability of intermediate sensors.
ISFAT [78]	TPS residuals + Diurnal integration	Hong Kong	3.33 K	Integrated three-sensor data required.
FSDAF [80]	Class-based unmixing + TPS	SW USA (40x40 km)	Lowest RMSE	Small spatial validation scope.
CFSDAF [81]	IDW + Soft classification	Beijing & Shenzhen	N/A	Optimized for urban but not agricultural areas.
LOTSFM [83]	Long-term regression + diff. term	Beijing; Shanghai; Guangzhou	1.6–2.17 K	Performance drops in dynamic agricultural areas.
Yao et al. [84]	Same-day partner sensor reconstruction	Beijing-Hebei; Pearl River Delta	$<$ 1.1 K (MAE)	Does not enhance spatial resolution.

to achieve the fusion. In computer vision, an image pyramid is used to represent an image at multiple resolutions simultaneously to separate details from broad trends. The method constructs two distinct pyramids to manage image resolution: the Gaussian Pyramid (the background) and the Laplacian Pyramid (the texture). The GLOSTFM model uses Microwave Radiometer (MWRI) data as the top layer of a Gaussian pyramid and progressively expands it downward through nearest-neighbor upsampling followed by Gaussian convolution smoothing, while injecting Laplacian textures at each level to reconstruct the finer layers at the bottom. Clear-sky MERSI LST images are used to extract the Laplacian spatial textures needed to sharpen the blurry microwave data. It takes the fine MERSI image and subtracts a smoothed, downsampled version of itself. spatial textures are then assumed to be constant based on the fact that streets, buildings, and water bodies form a spatially fixed and thermally stable environment. On the Cloudy Date, the model first corrects the microwave data for sensor differences (such as hardware and observation angles), then injects the extracted texture closest in time to this smooth microwave paint. The model achieved an average RMSE of 2.874 K for the MWRI–MERSI fusion. It was further evaluated using MWRI and MODIS observations, yielding RMSE values ranging from 5.1 K to 6.4 K. The larger errors in the MWRI–MODIS experiment are expected, as MWRI and MERSI are co-mounted on the same FY-3D satellite, whereas MODIS operates on NASA's Terra and Aqua platforms. Consequently, differences in observation time, viewing geometry, and sensor hardware introduce additional uncertainties that degrade fusion accuracy.

D. Machine learning based methods

Numerous machine learning techniques are applied for modelling LST and reconstructing missing pixels. As shown in Figure 11, these approaches are broadly categorized into classical machine learning and deep learning. Classical methods include ensemble learning, which aggregates multiple base learners—typically through bagging, boosting, or stacking—to enhance predictive robustness and generalization. This category also encompasses sparse and feature learning techniques designed to optimize data representation through dimensionality reduction. In contrast, deep learning architectures utilize multi-layered neural networks to autonomously extract hierarchical patterns from high-dimensional data. The following subsections detail the theoretical foundations of these paradigms.

1) Classical machine learning

Within the context of LST gap-filling, prominent classical methods include a variety of ensemble, sparse, and instance-based learners. Ensemble learning techniques, such as Random Forest (RF), Gradient Boosting Machine (GBM), and Extreme Gradient Boosting (XGBoost), are widely utilized; these models aggregate multiple decision trees to minimize predictive error and enhance robustness. Sparse learning and regularized methods, including Dictionary Learning and Lasso Regression, focus on identifying the most salient features and optimizing data representation to prevent overfitting. Additionally, traditional algorithms like Support Vector Regression (SVR) and k-Nearest Neighbors (kNN) provide effective non-linear and instance-based frameworks for spatial pixel reconstruction.

RF regression, in particular, has been extensively applied to reconstruct missing LST data due to its ability to model

TABLE V
SYNTHESIS OF REPRESENTATIVE TIR–PMW ALL-WEATHER FUSION METHODS.

Method	Core Fusion Mechanism	Study Region	RMSE (K)	Major Limitation
Duan et al. [86]	Deterministic downscaling via lapse rates + IDW.	Heihe River Basin, China	3.5–4.4	Artificial boundaries and grid effects at seams.
BME (Kou et al. [87]; Xu et al. [88])	Probabilistic Gaussian PDFs + Spatiotemporal covariance.	Tibetan Plateau; Heihe Basin	2.31–8.29	Excessive smoothness; high errors in rugged terrain.
CDF-MKF [89]	GWR downscaling + CDF matching + Kalman Filtering.	China (National scale)	3.00–3.82	Complex multi-stage processing requirement.
Dowling et al. [90]	Two-step: Regression filling + PMW bias calibration.	Kenya	2.6–3.6	Unsuitable for desert, snow, or ice regions.
GLOSTFM [91]	Computer vision: Gaussian and Laplacian pyramids.	Global evaluation	2.87–6.4	Sensitive to inter-sensor time/geometry offsets.

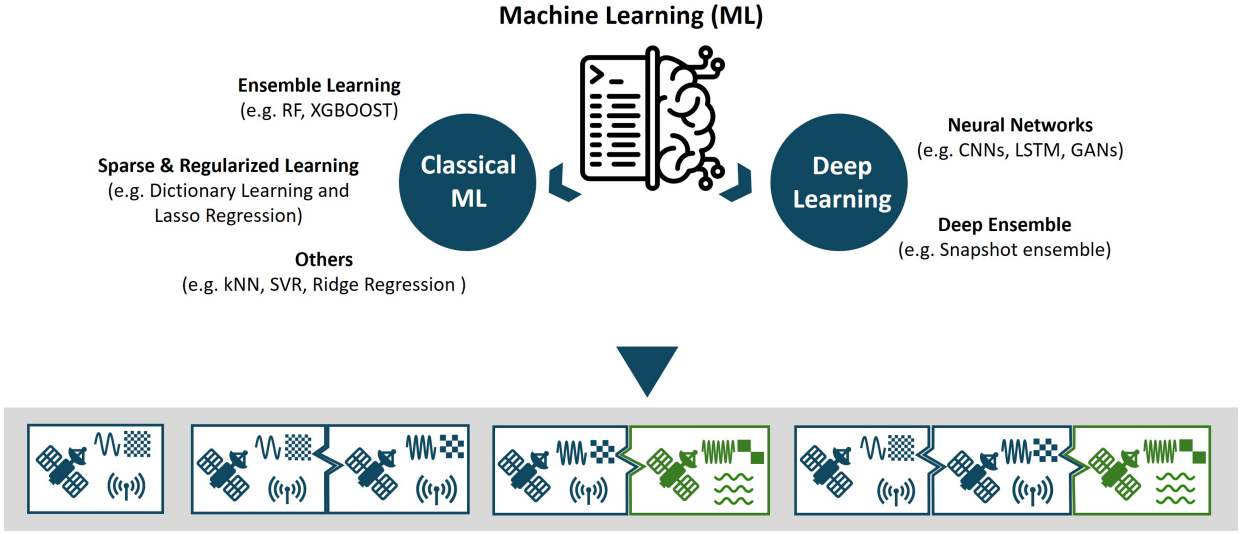

Fig. 11. Integrated machine learning frameworks for LST gap-filling

complex nonlinear relationships between LST and environmental predictors. Buo et al. [92] trained RF model to predict 1 km MODIS LST using a combination of temporal features (Day of the Year and Year), vegetation features (NDVI), and spatial covariates (surface types, mean elevation, distance to the coast, and coordinates). The model is trained for the region of Estonia during the summer months (May–August) of the years 2010, 2014, and 2018. The final RF model demonstrated strong predictive capability on the validation data, achieving RMSE of 1.46 K. Advancing this approach, Wu et al. [93] introduced the spatial feature-considered random forest regression (SFRFR) model, a hybrid of RF regression and Kriging regression. In this case, numerous spatial parameters are utilized to predict LST through RF regression, including soil texture (ST), population density (PD), digital elevation model (DEM), enhanced vegetation index (EVI), solar zenith angle (SZA), surface reflectance of the middle-infrared (MIR), and land use and land cover change (LUCC) data. The predicted LST is then corrected with a residual term, which is computed as the difference between the original LST and the RF prediction for valid (cloud-free) pixels, while Kriging interpolation is applied to estimate residuals for pixels with missing data. Trained on 100 m Landsat 8 LST data for Wuhan, China, the SFRFR model demonstrated high precision with an RMSE of 1.18 K for reconstructing artificially masked pixels, consistently outperforming standard RF regression. While Buo et al. [92] and Wu et al. [93] utilize spatial and temporal variables primarily as model inputs, Wang et al. [94] further refined the modeling architecture to explicitly account for the four-dimensional dependencies of LST—integrating horizontal and vertical space, elevation, and time. Evaluated on eighty-six Landsat-GOES image pairs across six regions in the United States from July 2017 to June 2021, this spatial–temporal RF (STRF) method yielded an average RMSE of 1.6444 K. Although this error is slightly higher than single-sensor reconstructions, it reflects the inherent complex-

ity of cross-sensor fusion and the environmental heterogeneity present across multiple large-scale regions. Building on these methodological advancements, further applications have demonstrated the adaptability of RF frameworks to diverse climatic conditions and varying data constraints. Chongtaku et al. [95] implemented an RF regression framework to reconstruct 1 km cloud-contaminated pixels in MODIS LST products across Thailand. By modeling nonlinear relationships between LST and variables such as elevation, land-use, and ground-based air temperature, the study revealed a distinct performance divergence based on the diurnal cycle: daytime models exhibited an RMSE of up to 5.02 K due to solar radiation variability, while nighttime models achieved a more stable RMSE of 2.09 K. Notably, they identified a shift in variable importance, with Day of the Year (DOY) dominating daytime predictions and minimum air temperature serving as the primary predictor at night. In the Heihe River Basin, Chen et al. [96] generated daily gap-free MODIS LST products using an RF framework centered on eight key environmental predictors, identifying elevation as the most influential factor. To maintain accuracy in heavily clouded imagery where clear-sky observations were sparse, they employed a hybrid RF-similar-pixel (RF-SP) interpolation scheme, which maintained a satisfactory RMSE of 6.37 K even under high cloud pollution (higher than 70%). Finally, Liu et al. [97] advanced the field toward multi-source integration by developing an ensemble of RF and Ridge Regression (RFRR) to fuse PMW and TIR data from the Fengyun-3C satellite. The methodology involved several sophisticated stages, including the use of Singular Spectrum Analysis (SSA) to fill orbital gaps in microwave data and Savitzky–Golay (S-G) filtering to produce continuous daily vegetation indices. These inputs were integrated into an innovative RF and Ridge Regression (RFRR) ensemble to model the complex nonlinear relationships between LST and six environmental variables—such as downscaled microwave LST, the Savitzky–Golay smoothed vegetation index (NDVI), land cover type, digital elevation model (DEM), terrain slope, and geographic coordinates. Accuracy evaluations confirmed RMSE of less than 2.3 K when validated against ground-based observations and MODIS products, with particularly robust performance noted in desert and marshland environments.

Despite the demonstrated flexibility and strong predictive performance of RF-based frameworks, these models do not explicitly enforce spatial smoothness or gradient continuity across reconstructed and observed regions. To address this limitation, a fusion of RF and HANTS predictions using the Poisson equation has been proposed [98]. The Poisson equation, a partial differential equation, enforces gradient continuity and ensures seamless transitions between reconstructed and valid pixels. This integrated framework was applied to generate clear-sky MODIS LST data over two study areas in China: Huainan (HN) in Anhui Province and Jining (JN) in Shandong Province, achieving high accuracy with RMSE generally below 2 K and often below 1.2 K in simulated scenarios.

Beyond Random Forest, other ensemble learning techniques like XGBoost have demonstrated high efficiency in all-weather LST generation. Duan et al. [85] proposed a framework to generate spatially seamless, all-weather 1-km LST by integrating MODIS LST and AMSR2 PMW LST. XGBoost was employed as the core ensemble regression algorithm to model LST heterogeneity using six environmental variables, including corrected PMW data, NDVI, land cover, DEM, slope, and climate classification. The framework was applied to the entire 366-day calendar year of 2020, with a total of 732 XGBoost models constructed, consisting of separate daytime and nighttime models for each day of the year. In-situ validation over the Heihe River Basin indicated that the daytime reconstruction achieved a ubRMSE of 4.54 K with a bias of 3.61 K, resulting in a total RMSE of 5.8 K. Notably, this performance represents a slight improvement over the RF-SP framework implemented by Chen et al. [96] in the same study area, which reported an RMSE of 6.37 K. This discrepancy suggests that the gradient boosting architecture of XGBoost, combined with the integration of AMSR2 PMW data, may offer superior capabilities in capturing LST heterogeneity under high cloud pollution compared to traditional RF-based interpolation schemes. Complementary to these findings, Li et al. [99] developed an XGBoost-based framework to estimate clear-sky LST at a 30 m spatial resolution across diverse vegetated landscapes. By integrating Synthetic Aperture Radar (SAR) and topographic data, the model captures the complex statistical relationships between Landsat-derived LST and a multi-source feature set. Specifically, the predictors include Sentinel-1 SAR polarizations (VH, VV) and the Radar Vegetation Index (RVI), complemented by topographic variables such as elevation, slope, and aspect. The framework's robustness was demonstrated across 29 dates in 2020 over six heterogeneous regions, including five sites across China (the Loess Plateau, Qinghai–Tibet Plateau, Northeast China Plain, North China Plain, and Nanling Mountains) and one in Nevada, USA. Comparative evaluations within the study indicated that XGBoost consistently achieves higher precision than traditional RF architectures. For instance, in a specific case study on 29 January 2020, the XGBoost-based radar-guided model achieved an RMSE of 1.296 K, outperforming the RF-based benchmark of 1.311 K. Collectively, these studies highlight a fundamental algorithmic advantage: while RF regression relies on an ensemble of independent decision trees to reach a prediction, XGBoost employs a sequential, additive learning process. By iteratively training weak learners to minimize the residuals of preceding models, XGBoost more effectively corrects prediction errors, resulting in more geophysically realistic LST reconstructions across varying spatial and temporal scales.

Apart from ensemble learning, sparse learning and regularized regression methods constitute another category of techniques for LST gap filling. Li et al. [100] employed dictionary learning to reconstruct cloud-contaminated MODIS LST products, proposing two multitemporal sparse models, expanded MT-KSVD and Bayesian MT-BPFA, that exploit temporal correlations to recover missing surface temperature information. The framework was evaluated using daily 1-km MODIS LST products over a seven-day period in 2012, covering consecutive days from the 67th to the 73rd day of the year. These experiments were conducted on 300 ×

300-pixel subregions cropped from georeferenced datasets. In scenarios of partial cloud corruption, where some valid pixels remain in the target image, the MT-BPFA model achieved an RMSE of 0.286 K, while the MT-KSVD model recorded an RMSE of 0.778 K. For complete corruption scenarios—where the entire subregion is obscured by thick clouds—the errors reached 1.872 K for MT-BPFA and 1.917 K for MT-KSVD. While MT-BPFA generally maintains higher precision when provided with sufficient auxiliary data, MT-KSVD is noted for being better suited to situations with limited data, despite exhibiting greater sensitivity to the initial dictionary. More recent advancements have adapted dictionary learning applied within the field of computer vision, specifically Example-Based Super-Resolution (SRR) originally proposed by Freeman et al. [101] to enhance low-quality photos. The proposed method generates gap-free high-resolution all-weather LST, without using any auxiliary data, only by downscaling coarse-resolution Microwave data (AMSR-E at 25 km or AMSR-2 at 10 km) to fine-resolution TIR data (MODIS at 1 km or GOES at 4 km). The downscaling is achieved by learning from a dictionary of paired high- and low-resolution image patches derived from historical clear-sky MODIS/GOES observations. To ensure the resulting 1 km or 4 km grids are spatially coherent and free of checkerboard artifacts, the method employs a Markov network and Belief Propagation to model the compatibility between neighboring patches. The study utilized data from 2008 (for the AMSR-E and MODIS fusion) and 2015 (for the AMSR-2 and GOES fusion). Evaluated against ground measurements from the SURFRAD network, the model achieved an RMSE of approximately 4 K. The authors note that this error is very similar to the native error of the original coarse Microwave data. This implies that the downscaling process itself added very little error; it simply inherited the uncertainty of the microwave sensors while successfully improving the spatial resolution [102].

In contrast to sparse representation-based approaches, Zhou et al. [103] developed a regularized regression framework for Landsat LST gap filling based on LASSO linear regression, which leverages data redundancy in orbit overlap regions. The methodology employs K-Means clustering and stratified random sampling to identify training pixels with seasonal patterns similar to the target pixel. By employing LASSO linear regression across ten iterations and utilizing the aggregated median, the framework generates stable 30-m resolution predictions alongside uncertainty estimates. Tested on 2018 data from Atlanta, Georgia, this regularized framework achieved an average RMSE of 3.88 K.

In a comparative assessment of classical machine learning performance, Mishra et al. [104] compares RF, GBM, SVR, and kNN for generating LST at a fine spatial resolution of 10 m by combining Landsat 8 thermal data (30 m) with fine-scale Sentinel-2 optical data in Varanasi, India. Their comparative analysis identified GBM as the top-performing model. The authors further concluded that ensemble-based methods, such as GBM and RF, generally outperform linear frameworks such as LASSO for high-resolution LST generation, because of their ability to model complex nonlinear relationships. Conversely, kNN proved to be the least effective of the four techniques. This hierarchy of performance, however, may be task-dependent, as demonstrated by Sarafanov et al. [105] through their SSGP-toolbox, which supports LST gap-filling using RF, kNN, SVR and LASSO. In their evaluation on 1 km Sentinel-3 LST and MODIS Terra LST across diverse geographical regions, including Saint Petersburg, Madrid, and Vladivostok, the authors found that SVR was the most accurate method specifically for filling. Notably, the SSGP-toolbox evaluation did not include GBM, which may account for the divergence in results between the two studies. Nevertheless, these findings suggest that while SVR may excel in the spatial restoration of coarser 1-km data, hyperparameter-tuned ensemble methods like GBM are superior for bridging temporal frequency gaps and downscaling to 10-m resolutions within the complex thermal dynamics of urban environments like Varanasi. Ultimately, this comparison highlights how the optimal model is determined by the specific nature of the data gaps addressed and the environmental complexity of the study area.

The architectural diversity of classical ML frameworks, ranging from ensemble learners to sparse dictionary methods, is synthesized in Table VI.

2) Deep Learning

While linear and ensemble-based frameworks remain widely utilized for their robustness and efficiency, DL has emerged as a powerful alternative for LST gap filling, particularly in scenarios requiring the modeling of intricate spatiotemporal dependencies. Through architectures like CNNs, RNNs, and GANs, DL enables the autonomous extraction of features. Recent advancements have seen a shift toward specialized structures, including U-Net variants for precise image-to-image restoration and hybrid frameworks that integrate DL with physical or classical statistical model. The technical progression of deep learning architectures is synthesized in Table VII, highlighting the shift toward multi-stage fusion and high-resolution image-to-image translation.

This subsection will review the progression of these deep learning architectures, beginning with temporal and spatial feature extraction models, followed by advanced encoder-decoder networks and generative approaches, and concluding with recent hybrid frameworks that integrate deep learning with auxiliary data and classical algorithms.

Among the earliest deep learning efforts for LST reconstruction were recurrent architectures designed to leverage temporal dependencies, Arslan and Sekertekin [106] used LSTM to reconstruct daily MODIS LST data in Ceyhan, Adana; an agricultural area in Turkey, using time-series data from January 2017 through February 2019. The reported RMSE values against artifically masked pixels ranged from 2–9 K for daytime observations and 1–5 K for nighttime observations. Although the authors did not explicitly provide a single average RMSE for the entire dataset, the highest reported daytime error (9 K) appears to represent an outlier rather than typical performance. Most daytime RMSE values were concentrated around 4–5 K, while nighttime errors were predominantly within the 1–3 K range. Despite these results, this approach remains low-performing compared to the other deep learning methods discussed in this section, illustrating

TABLE VI
SYNTHESIS OF REPRESENTATIVE CLASSICAL MACHINE LEARNING METHODS FOR LST GAP-FILLING.

Category	Specific Method & Logic	Study Region	RMSE (K)	Major Limitation / Insight
SFRFR [93]	Ensemble Learning: RF + Kriging residual correction.	Wuhan, China	1.18	Hybridizing RF with spatial interpolation improves gradient continuity.
STRF [94]	Ensemble Learning: RF-based model integrating 4D (horizontal, vertical, elevation, time) dependencies.	USA (6 regions)	1.64	Higher error reflects complexity of cross-sensor environmental heterogeneity.
RF-SP [96]	Ensemble Learning: RF + similar-pixel interpolation.	Heihe River Basin	6.37	Maintains stability even under high (¿70%) cloud pollution.
XGBoost [85], [99]	Ensemble Learning: Sequential additive learning for error correction.	China; Nevada, USA	1.29–5.8	Iterative boosting generally captures heterogeneity better than independent RF trees.
MT-BPFA [100]	Sparse Learning: Dictionary learning via temporal correlations.	Regional subregions	0.28–1.87	Precision drops significantly in complete corruption (thick cloud) scenarios.
SRR [102]	Sparse Learning: Example-based super-resolution from clear-sky patches.	USA (SURFRAD)	4.0	Inherits native sensor error from coarse microwave inputs.
LASSO [103]	Regularized Regression: Redundancy leveraging in orbit overlap regions.	Atlanta, USA	3.88	Struggle to model complex nonlinear relationships compared to ensembles.
SVR / kNN [104], [105]	Non-linear frameworks for spatial reconstruction.	India; Spain; Russia	2.22–2.71	SVR excels in 1-km spatial restoration, but kNN is often the least effective.

the limitations of relying solely on temporal sequences.

Building on this understanding, later studies increasingly leveraged convolutional architectures to better capture spatial structures in remotely sensed imagery. CNN-based approaches for LST reconstruction have transitioned from basic encoder-decoder structures to complex multi-source fusion and attention-gated networks. An early milestone in this progression was the Multiscale Feature-Connected CNN (MFCTR-CNN) proposed by Wu et al. [49], which extends the standard encoder-decoder architecture by concatenating target and auxiliary images to capture joint spatiotemporal dependencies. To mitigate the smoothing common in deep networks, MFCTR-CNN employs skip connections via Spatial Attention Units (SAUs) and incorporates average pooling to enlarge the receptive field. Furthermore, a residual learning strategy ensures the model reconstructs only missing values while preserving original observations. Evaluated on hourly 5-km FY-2G data in China and 15-minute 3-km MSG-SEVIRI data across Europe, the model maintained an average RMSE below 0.8 K even with 70% cloud cover. Expanding on the capability of CNNs for data integration, Xue et al. [107] developed a multi-source fusion framework designed to reconstruct a nine-year (2000–2008) archive by merging MODIS Terra and Aqua LST products. Rather than relying on standard loss functions, they utilized a Normalized Cross Correlation (NCC) loss to better preserve structural integrity and high-frequency spatial details. This approach optimized high-quality pixel coverage by 6.2% and recovered up to 23% more usable data compared to the raw satellite imagery. Addressing the inherent trade-off between spatial and temporal resolutions, Yin et al. [108] developed the Spatiotemporal Temperature Fusion Network (STTFN). This multi-stage CNN architecture is designed to fuse high-temporal MODIS data with high-spatial Landsat imagery. The STTFN framework utilizes a specialized super-resolution module to upscale coarse features and a spatiotemporal-consistency (STC) weighting mechanism to ensure that the synthetic high-resolution LST remains physically consistent with the temporal trends of the input series. Evaluated against traditional fusion algorithms like ESTARFM, STTFN demonstrated superior performance with an average RMSE below 1.40 K and higher structural similarity, proving that multi-stage deep learning can more effectively capture the complex thermal heterogeneities of the land surface than weight-based linear fusion methods. Further advancing this lineage, Li et al. [109] developed the Spatio-Temporal Attention Network (STAN). Built upon a U-Net backbone, STAN augments the feature extraction process with a non-local module to capture long-range spatial relationships and a squeeze-and-excitation (SE) module to align channel-wise features with the diurnal variability of LST. Unlike MFCTR-CNN, which primarily captures coarse spatial distributions, STAN enhances the reconstruction of heterogeneous LST patterns by integrating auxiliary ground-based meteorological variables, DEM data, and land cover ratios. Under identical experimental conditions, STAN consistently outperformed MFCTR-CNN, reducing the RMSE from 1.16 K to 0.91 K in a standardized 24-hour evaluation.

Another application of CNNs is the refinement of data that

has been gap-filled using the enhanced ATC model. The hybrid ATC-3DCNN approach, developed by Fu et al. [110], employs a three-dimensional convolutional kernel that simultaneously slides across spatial and temporal dimensions. This method was applied to gap-fill both MODIS and Landsat LST data over Beijing, China, achieving RMSEs of 0.61 K and 0.96 K, respectively.

Substituting standard convolution layers with partial convolutions in a U-Net architecture was first proposed by Liu et al. [111] for the inpainting of irregular holes. While standard convolution applies uniformly across all input pixels, partial convolution incorporates a binary mask and a mask update mechanism, allowing it to selectively operate only on valid pixels. This technique was adapted by Chen et al. [112] who introduced the Source Augmented Partial Convolution v2 model (SAPC2) for the inpainting of Landsat 8 LST. The model was trained and validated on data from 2014 to 2018 in Colorado, USA. Notably, because SAPC2 utilizes a unitless MSE on standardized data to prioritize spatial textures, direct comparison with absolute temperature metrics is challenging; a rigorous benchmark would require re-evaluating the model on raw temperature values to derive an RMSE in Kelvin. Additionally, Huber et al. [113] implemented partial convolution within a U-Net architecture to interpolate missing pixels and generate daily gap-free MODIS LST data at 1 km spatial resolution. As a preprocessing step, air temperature data from weather stations were mapped to the equivalent surface temperature values using a linear regression model to provide initial estimates for invalid pixels. Their approach was applied to a wine-growing region in Rhineland-Palatinate, Germany, covering the period from 11 March 2008 to 15 November 2022, achieving RMSE of 1.67 K.

Beyond standard reconstructive CNNs, recent research has explored the potential of image-to-image translation for high-resolution LST estimation. Khedher et al. [114] introduced a novel multimodal approach that is uniquely distinguished by its ability to translate non-thermal RGB orthophotography and auxiliary variables into fine-scale thermal maps. Utilizing a conditional Generative Adversarial Network (cGAN) based on the pix2pix architecture, the methodology employs a U-Net generator to process multi-channel tiles of RGB imagery, DEM, and land cover data, while a discriminator critiques the realism of the generated transformations. A defining feature of this approach is the generation of LST at an ultra-high spatial resolution of 1 meter—a level of detail rarely achieved in existing LST literature. In a case study conducted in the Lyon Metropolis, France, the model was applied to the resolution-enhancement and imputation of Landsat 8 data, achieving a mean RMSE of approximately 1.5 K in urban zones. The authors attribute this precision to the synergy of data modalities; specifically, the inclusion of land-cover data enabled the model to distinguish thermally distinct surfaces that appear identical in the visible spectrum, such as natural versus synthetic turf. Despite these promising results, the authors acknowledged that the resulting imagery often exhibited visible seams or blocking artifacts at the boundaries of the 256×256-pixel tiles. Furthermore, while the authors noted that further investigation is required to determine the model's performance under different conditions, the current reliance on a single-day test suggests that the framework's generalizability across diverse climatic and seasonal contexts remains to be fully established. To address the spatial discontinuities identified in the initial work, a subsequent study by Khedher et al. [115] introduced the RGB2LST framework. The methodology utilizes a 50% overlapping tiling strategy during the preparation of the 1-meter resolution dataset to ensure spatial continuity across the generated tiles. This advanced approach, trained on an expanded dataset of over 22,000 tiles, achieved a normalized RMSE of 0.062. Crucially, the study found that while a simple arithmetic averaging of the overlapped estimated pixels improved quantitative metrics, it was insufficient for artifact suppression. Instead, the authors implemented a weighted fusion method based on a Truncated Gaussian Function to handle the overlapping regions. By assigning higher weights to centrally located pixels within a tile and gradually decreasing weights toward the boundaries, this approach successfully eliminated visible seams. Collectively, these studies illustrate a significant conceptual shift from conventional gap-filling techniques, demonstrating that fine-scale thermal structures can be inferred from the spatial and spectral cues embedded in high-resolution optical imagery.

Rather than relying on either CNNs or GANs in isolation, the Two-step Deep Learning Framework (TDLF) proposed by Wu et al. [116] explicitly integrates both architectures within a unified pipeline. In the first stage, a CNN is employed to fill swath gaps in AMSR-E PMW data, while in the second stage, a GAN-based network fuses the reconstructed PMW data with TIR observations to generate a gapless, all-weather MODIS LST product. The framework was validated over regions in China, specifically the HRB and TP regions, achieving RMSE of 1.71–2.0 K against in-situ measurements under clear-sky conditions and an RMSE of 3.41 K to 3.87 K when validated against in-situ measurements under cloudy conditions.

E. Physics enhanced methods

Incorporating physical principles that govern heat exchange at the Earth's surface supports accurate LST estimation. While purely data-driven models demonstrate strong performance in pattern recognition, they often lack the thermodynamic constraints required to ensure that reconstructed values remain physically plausible. This section therefore examines approaches that move beyond statistical correlation by integrating physically based information into the reconstruction pipeline. The following subsections review how physical information is used to support LST reconstruction across a range of methodological paradigms, from deterministic and statistical formulations to classical machine learning frameworks and physics-guided deep neural network architectures, following the conceptual integration pathways illustrated in Figure 12.

1) Physically Enhanced Statistical and Deterministic Approaches

Jin [117] established a foundational SEB-based framework for retrieving cloudy-sky temperatures, introducing a cloudy-pixel treatment that remains a benchmark for physically-consistent reconstruction. The proposed methodology adopts

TABLE VII
SYNTHESIS OF REPRESENTATIVE DEEP LEARNING METHODS FOR LST GAP-FILLING.

Method	Technical Description	Study Region	RMSE (K)	Major Insight / Perspective
Arslan & Sekertekin [106]	RNN (LSTM): Leverages sequential temporal dependencies to reconstruct daily MODIS LST.	Turkey	1.0–9.0	High error (up to 9 K) highlights the limits of relying solely on temporal sequences.
MFCTR-CNN [49]	Encoder-Decoder CNN: Multi-scale feature connection and skip connections via Spatial Attention Units (SAUs).	China; Europe	¡ 0.8	Reconstructs missing values while preserving original observations via residual learning.
ATC-3DCNN [110]	Hybrid CNN: Employs a 3D convolutional kernel sliding across spatial and temporal dimensions.	Beijing, China	0.61–0.96	Effectively refines data previously gap-filled using physical ATC models.
SAPC2 [111], [112]	Partial CNN: Uses binary mask updates to selectively operate on valid pixels and preserve spatial textures.	Colorado, USA	N/A*	Selective masking prevents standard convolution smoothing of valid pixels.
STAN [109]	Attention-Gated CNN: U-Net backbone with non-local spatial and SE channel-wise feature alignment.	Global or Regional	0.91	Superior capture of heterogeneous patterns compared to standard CNN architectures.
RGB2LST / pix2pix [114], [115]	cGAN: Translates RGB orthophotography and DEM into 1-m resolution thermal maps.	Lyon, France	1.5	Demonstrates that ultra-high resolution thermal structures can be inferred from optical cues.
TDLF [116]	Multi-Stage (CNN+GAN): CNN fills PMW swath gaps; GAN fuses reconstructed PMW with TIR observations.	China (HRB/TP)	1.71–3.87	Two-step pipeline provides robust all-weather capability under high cloud cover.

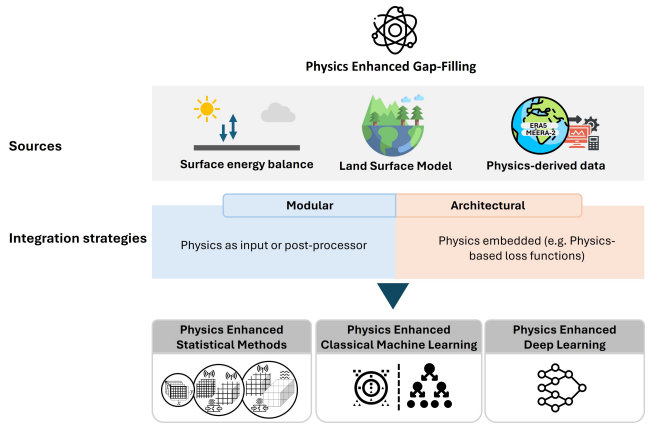

Fig. 12. Conceptual design of physics-enhanced frameworks for LST gap-filling

a dual-path hybrid architecture that prioritizes a Neighboring-Pixel (NP) strategy, with surface air temperature (SAT) adjustment serving as a complementary fallback mechanism. In the NP component, the SEB is parametrized as a function of LST to formulate temperature differences between two neighboring pixels, allowing missing values to be estimated as a weighted sum of surrounding clear-sky pixels with similar vegetation, soil, and topographic characteristics within a prescribed spatial distance. In scenarios where the NP approach is unfeasible—typically due to extensive cloud persistence—the framework employs an air temperature adjustment based on Monin-Obukhov similarity theory, mapping near-surface air temperatures (1.5–2.0 m) to their equivalent surface skin temperatures. While the framework demonstrated an accuracy of 1–2 K at a monthly mean resolution across diverse climatic gradients in North America and Europe, its sensitivity to seasonal and land-cover variations led to further refinements. Yu et al. [118] addressed these limitations by implementing a parameter regionalization strategy within the Heihe River Basin. By substituting generalized empirical coefficients with site-specific parameters derived from long-term observations, they enhanced the model's sensitivity to localized environmental dynamics. However, the validation against on-site measurements revealed that achieving localized physical consistency does not always guarantee low variance; the reconstructed daytime LST yielded an RMSE of 4.122 K, while the nighttime reconstruction, benefiting from the absence of shortwave radiation complexity, achieved a more stable RMSE of 2.901 K.

Subsequent studies have critiqued traditional SEB-based approach for being oversimplified by focusing on instantaneous energy balances and using static coefficients, which can propagate and amplify errors from uncertainties in the input forcing data. To overcome these limitations by shifting the focus from instantaneous to cumulative dynamics, Xu et al. [119] introduced the Cloud-regulated Surface Warming Model (C-SWARM). The C-SWARM model reconstructs all-

weather daytime LST through a structured multi-temporal workflow that shifts from modelling instantaneous energy transitions to characterising a cumulative surface warming process starting from sunrise. The operational sequence begins by estimating the sunrise LST using a linear regression strategy based on near-surface air temperature, leveraging the physical principle that overnight insulation brings these two temperatures into close alignment by dawn. Subsequently, the model quantifies the cloud effect by calculating the difference in surface energy budgets between the target cloudy day and a clear-sky reference day identified within a sliding temporal window. This quantification is driven by two primary physical kernels: cumulative solar heating power, which accounts for the shading effect of clouds on sunlight, and atmospheric thermal insulation, which proxies the thermal exchange between the ground and the atmosphere. By applying intraday-variable coefficients calibrated in 1-hour increments, the model captures the shifting interplay where solar radiation dominates surface warming at midday while atmospheric insulation becomes the primary driver later in the afternoon. The final all-weather LST is reconstructed by summing the estimated sunrise temperature, the clear-sky LST change, and the modelled Cloud Effect, providing a physically explicit solution that remains resilient to uncertainties in input data. Validated across the contiguous United States (CONUS) using NOAA's GOES-R geostationary data, the model demonstrated high physical resilience, achieving a mean RMSE of 3.43 K across 20 independent trials.

Parallel to these developments, other studies have advanced hybrid frameworks that integrate statistical spatiotemporal interpolation with physically grounded SEB-based model products, such as LSM and atmospheric reanalysis data. Güngör Şahin and Gündüz [120] developed an LST gap filling framework that integrates multi-source satellite observations (MODIS and VIIRS) with model-based data (GEOS-5 Catchment Land Surface Model (CLSM)) to generate spatially seamless 1 km resolution maps. First, approximately 10–15% of the data gaps are filled by merging the different satellite observations (VIIRS VNP21, MODIS Aqua, and MODIS Terra) using sequential linear regressions. Then, a linear regression model was fitted to determine the specific slope and bias between the satellite-derived observations and the CLSM model-based data on a seasonal basis. Missing pixels were filled with these corrected CLSM values. A major highlight of this approach is its high accuracy and simplicity. Validated on Western Anatolia Basin (WAB), located in the Aegean Region of Türkiye, the reconstructed product achieved an RMSE of 1.84 K across the 2019–2022 study period. In a related move toward physically enriched interpolation, Shi et al. [121] introduced the Multivariate Data Interpolating Empirical Orthogonal Functions (MDINEOF), a significant advancement of the standard DINEOF algorithm. While traditional DINEOF relies on EOF decomposition of LST alone, MDINEOF incorporates a multivariate stacking approach. By vertically stacking LST with physically-governed radiation variables, specifically all-sky longwave downward radiation (LWDR) and all-wave net radiation (AWNR), the algorithm exploits the intrinsic physical correlations between surface temperature and radiative forcing. This multidimensional architecture allows for the reconstruction of all-weather (cloudy-sky) LST based on latent physical relationships rather than the statistical interpolation of clear-sky assumptions. Consequently, MDINEOF represents a transition from purely mathematical gap-filling to a physically-supported framework capable of capturing the thermal dynamics of the land surface under cloud cover. The incorporation of radiation fluxes allowed MDINEOF to reduce the RMSE from 6.86 K to 3.28 K relative to the original DINEOF method, when both were evaluated against in-situ measurements using MODIS data. Similarly, Ma et al. [24] developed an integrated temperature fusion framework to produce gapless LST maps at 60-m spatial resolution and half-hourly temporal resolution for urban-dominated region (Wuhan, China) and a natural-dominated region (Heihe River Basin, China) by blending Landsat and MODIS observations with SEB-informed CLM 5.0 simulations. The model operates through a three-step workflow that involves selecting similar pixels within a predetermined moving window, determining a spatio-temporal weighting function, and finally estimating the fine-resolution LST for the predicted time. The fused all-weather LST showed an RMSE of 0.97–1.26 K against actual clear-sky Landsat LST and a broader RMSE range of 1.09–4.36 K against in-situ measurements.

To move beyond the constraints of spatial pixel-matching, alternative hybrid approaches leverage the inherent periodicity of surface temperatures by integrating Annual and Diurnal Temperature Cycle (ATC/DTC) models with reanalysis data. For example, Hong et al. [122] proposed the ADTC-based framework to generate gap-free, all-weather LST. The framework sequentially combines an enhanced ATC model, represented by a single sinusoidal function constrained by daily surface air temperature from MERRA-2 reanalysis to capture day-to-day variability, with a DTC model. The spatiotemporal continuous daily mean LST is obtained by first applying the enhanced ATC to estimate the daily conditions, which are then used to reconstruct instantaneous under-cloud LST and fill gaps across the four daily satellite overpass times. Subsequently, a four-parameter DTC model was fitted to the combined clear-sky and reconstructed observations to simulate the full 24-hour temperature cycle. The gap-filled MODIS LST products were validated against geostationary satellite observations (FY-2F and MSG-SEVIRI) for cloud-free diurnal cycles and in-situ measurements from the SURFRAD network under overcast conditions, achieving a daily MAE of approximately 1 K.

While the aforementioned hybrid models rely primarily on spatial and statistical interpolation principles, recent advancements have introduced dynamic data assimilation to achieve global coverage. Jia et al. [123] proposed a framework that integrates multi-satellite observations with physically-based modelling to generate global hourly, 5 km, all-weather LST dataset for the period 2011–2021. The framework first builds a time-evolving model using ERA5 clear-sky scenarios to provide continuous signals of how temperature changes over time due to air movement and weather shifts, even when the surface is hidden by clouds. Then, clear-sky LST observations from multi-stattlite are blended into this model using a Kalman

filter resulting in a complete map of hypothetical clear-sky LST. Finally, the cloud cooling and warming effects are quantified using Clouds and Earth's Radiant Energy System (CERES) radiation products and SEB equations. Evaluated against ground measurements from 201 global sites, including SURFRAD, BSRN, and Fluxnet, the resulting product demonstrates high accuracy with an overall hourly RMSE of 3.31 K and a daily mean RMSE of 1.76 K.

As a second physics-assisted approach with a global focus, Yu et al. [124] proposed a method that uses the statistical approach, DINEOF, to reconstruct a clear-sky baseline, and then uses the physics-derived ERA5-Land data to correct that baseline to all-weather conditions using a CDF matching-based correction method. The approach was validated across 17 global regions representing different land covers and 12 in-situ sites (located in the USA and China). The experimental results showed that the method achieved RMSEs of 1–2 K under ideal clear-sky conditions and RMSEs of 4–7 K under all-weather conditions.

In summary, while foundational models such as Jin [117] achieved RMSEs of 1–2 K, these results were aggregated at monthly mean resolution, inherently smoothing stochastic errors present in daily or hourly retrievals. At finer temporal scales, localized heterogeneity becomes more influential; for example, Yu et al. [118] and Ma et al. [24] demonstrate that models may show high precision against other satellite products (RMSE ¡ 1.3 K) but exhibit substantially higher errors when validated against in-situ measurements, reaching 4.1–4.4 K during daytime peaks. This discrepancy highlights a fundamental challenge: strong satellite-to-satellite performance does not guarantee absolute accuracy or universal spatial transferability. Even physically guided frameworks remain sensitive to site-specific dynamics and the representativeness error of station observations.Consequently, although hybrid and SEB–informed approaches can generate physically consistent all-weather LST products, their operational reliability is strongly contingent on the quality of the underlying reanalysis data and the robustness of site-specific parameterization. Low RMSE values achieved within a given region or climate zone therefore cannot be assumed to generalize globally. Nevertheless, the integration of dynamic data assimilation such as the Kalman filtering of time-evolving ERA5 signals implemented in [123] offers promising prospects for advancing global-scale, all-weather modeling.

2) Physically Enhanced Classical Machine Learning Frameworks

While the physics-enhanced spatiotemporal interpolation and data assimilation frameworks discussed previously provide robust pathways for reconstruction, a distinct branch of research has emerged in parallel that leverages physics-enhanced classical machine learning. This direction is motivated by the limitations of pure machine learning methods, which are empirically based and rely heavily on massive training datasets, often failing to transfer well to data-sparse regions because they learn correlations rather than causations [125].

Guo et al. [126] utilized GAM to fill MODIS LST gaps in high-latitude cold regions by incorporating ERA5 Land Skin Temperature (ERA5ST) alongside satellite-derived environmental indices like NDVI and NDWI. While this method effectively captured seasonal variations, achieving an RMSE of approximately 2.7 K in the growing season and 3.4 K in the snowing season, it highlighted that reanalysis data often underestimates LST compared to satellite observations. Similarly, Dumitrescu et al. [127] applied a GAM framework to SEVIRI data, using ERA5ST as the primary predictor. Their GAM2 model, which accounted for the distance to missing pixels, outperformed standard multiple linear regression, achieving seasonal RMSEs between roughly 2.32 K and 2.60 K. Critically, while GAMs offer better interpretability and flexibility than simple linear models, they rely heavily on the resolution and quality of the underlying reanalysis data, effectively downscaling the physical model outputs using statistical relationships.

Moving toward ensemble learning, Zhang et al. [128] proposed the estimation of gap-free all-weather MODIS LST over the TP region for 2003 and 2014 using GLDAS LST reanalysis data to account for the effect of clouds on incoming shortwave radiation. The method estimates clear sky LST as the sum of ATC-derived temperature and a residual term estimated by an RF model trained to predict the residual given 10 descriptors including DEM, NDVI, solar zenith angle, and surface albedo. Validation against ground measurements showed the RTM LST has RMSE of 2.03–3.98 K. Moving beyond the use of reanalysis as a post-correction tool, Chen et al. [129] integrated physics-derived reanalysis data directly into the model training. They developed an RF-based method that utilized ERA5 surface downward shortwave radiation to physically constrain LST reconstruction under cloudy conditions. Radiation is fed directly into the RF model alongside vegetation indices and topography to predict the final LST. This approach achieved relatively high accuracy in mountainous terrain with an RMSE of 1.64 K to 1.72 K, demonstrating that incorporating radiative terms can help the model distinguish between clear and cloudy thermal dynamics.

However, while RF provides a robust foundation for integrating physical covariates, its ensemble averaging can attenuate sharp thermal fluctuations in heterogeneous landscapes; in contrast, the iterative boosting strategy of XGBoost is more effective at capturing high-frequency land-surface thermal responses to rapidly varying environmental drivers. In this context, Tan et al. [130] proposed an XGBoost approach that used soil surface temperature and soil moisture from the China Land Data Assimilation System (CLDAS) as physical linking variables. While this captured the thermodynamic state of the surface, the method yielded a relatively high RMSE of 4.42–4.97 K when validated against in-situ measurements. A more physics-intensive approach was taken by Xu et al. [131], who combined XGBoost with a Cloud Radiative Effect (CRE) model based on SEB equations. By explicitly calculating the energy budget using ERA5 data, they achieved an RMSE of 3.31–4.06 K over the Tibetan Plateau. Zhang et al. [132] further advanced this by using Bayesian Optimized XGBoost (BO-XGB) to estimate a hypothetical clear-sky LST, followed by an analytically derived physical correction for the cloud effect. This framework achieved a superior RMSE of 2.60 K over the US, suggesting that integrating analytical physical laws

(force-restore model) with machine learning offers a robust pathway to reduce the black box nature of pure ML models and improve accuracy beyond purely empirical approaches.

Beyond Random Forest and XGBoost, a range of physics-informed extensions and hybrid strategies have been proposed, including Light Gradient Boosting Machine (LightGBM)–based frameworks. Cho et al. [133] employed LightGBM with meteorological analysis data from the Local Data Assimilation and Prediction System (LDAPS), achieving an RMSE of 2.41–3.00 K for cloudy skies, noting that LightGBM offered significant computational speed advantages over RF. Building on this direction, Ma et al. [125] introduced a Mechanism-Guided LightGBM (MG-LGBM) that used causal inputs from the Community Land Model (CLM) to guide the learning process, achieving a cloudy-sky RMSE of 2.91–3.66 K. Finally, Zhang et al. [134] developed a multi-stage framework to generate 1-km all-weather LST by fusing PMW and TIR LST (FY-3B MWRI and MODIS), utilizing physical modeling to ensure temporal consistency between different satellite sensors. While the framework employed statistical methods like SSA to fill spatial swath gaps in the microwave data and RF for non-linear mapping of the coarse-resolution microwave data to the fine-resolution MODIS LST, its critical physical component was the application of a Diurnal Temperature Cycle (DTC) model derived from LDAS air temperature to physically adjust the microwave brightness temperatures to match the exact overpass time of the thermal sensor prior to data fusion. This physical fusion achieved an RMSE of 1.45–3.36 K against ground measurements, though the results highlighted that the accuracy of the reconstructed LST is highly correlated with soil moisture and land cover. The method performed best over water bodies, where microwave penetration depth is negligible, and recorded higher errors over barren desert sites (RMSE up to 3.25 K) in arid regions, where deep microwave penetration complicates the alignment between the skin temperature and the subsurface signal.

Another approach by Rolland et al. [135] demonstrates the combined advantage of computer vision techniques and physics-derived data through the development of GraphProp, a graph-based learning method designed to generate gap-free, clear-sky LST data. Distinct from traditional interpolation, this algorithm reconstructs the missing data in raw spectral bands rather than estimating the final temperature values directly. LST values are subsequently estimated by applying the Statistical Mono-Window algorithm, which integrates additional auxiliary physical data, including satellite-derived surface emissivity and atmospheric water vapor content quantified using NCEP/NCAR Reanalysis Data. The algorithm starts with graph Construction, where a structural representation of the region is built using a historical cloud-free reference image to create a k-nearest neighbors graph. Instead of relying on spatial proximity, this graph connects pixels based on their spectral similarity across nine Landsat 8 bands, allowing physically distant but spectrally similar areas to be mathematically linked. Once the graph is established, a finite difference approximation to heat diffusion is applied to propagate spectral information from observed, clear-sky nodes into the cloud-obscured regions. By holding observed values fixed, the algorithm solves for a steady state where the missing pixel values converge to the feature average of their spectral neighbors. Validation against synthetically introduced gaps on Landsat 8 across six diverse urban locations, including Jakarta, London, Paris, Cairo, Gaborone, and Québec City. Rather than a continuous calendar period, the experimental design utilized pairs of Landsat acquisitions (one reference and one target) separated by temporal gaps ranging from 2 to 20 weeks. Under extreme scenarios with 90% cloud cover, the method proved highly robust, maintaining an MAE below 1.8 K across all sites.

3) Physics-Guided Deep Learning Architectures

The evolution of LST reconstruction has seen a clear progression in how physical knowledge is utilized. While most physically enhanced statistical methods and classical machine learning frameworks discussed previously incorporate physical laws primarily as external inputs or post-processing constraints, physics-enhanced deep learning represents a transition from modular to architectural integration. Although these deep learning methods continue to utilize physical models as inputs for data fusion and effectively perform corrections through residual modeling, the state-of-the-art has moved beyond treating these as separate, external steps. Instead, modern frameworks embed physical equations directly into the neural network architecture and utilize physics-based loss functions to constrain the training process itself.

Within this domain, CNNs have been extensively adapted as the core architectural backbone, with physical components incorporated to explicitly encode physically meaningful spatial relationships. A notable example is the Nonlocality-Reinforced Network (NRN) developed by Gong et al. [136]. This framework employs a multiscale encoding–decoding U-Net architecture augmented with a nonlocality-reinforced attention module to reconstruct missing LST data by fusing MODIS observations with physics-based CLDAS assimilation data. The integration of nonlocal attention addresses a key limitation of standard CNNs, which predominantly capture local dependencies within immediate neighboring pixels. Since LST is a spatially continuous variable, distant regions often exhibit strong correlations due to shared physical attributes, such as similar elevation zones or land cover. By implementing these attention modules, the NRN enables a more effective mapping from coarse-resolution physical assimilation data to fine-scale satellite observations. This physically constrained spatial logic resulted in high reconstruction accuracy, achieving an RMSE of 0.7622 K when utilizing the full combination of input data—a comprehensive fusion that integrates the CLDAS daily ground temperature (providing a physics-based thermal baseline) with surface descriptors (NDVI and DEM) and auxiliary multi-temporal satellite LST products (8-day composite MOD11A2 and daily MYD11A1) to maximize spatiotemporal complementarity.

Similarly, Kustura et al. [137] integrate physics primarily by selecting specific input data that represent fundamental physical properties or processes. Notably, the input data are selected to reflect parameters of an LST empirical formula from micrometeorology literature that is derived from the energy balance equation. Their model does not require LST

as an input feature; instead, it learns to generate LST solely from meteorological and surface reflection data. The network is fed INCA meteorological data (Air Temperature, Global Radiation, Relative Humidity, and Wind Speed) to represent atmospheric forcing, alongside Sentinel-2 and land cover data to represent surface properties and the Bowen ratio. The Bowen ratio, defined as the ratio between sensible heat (heat that raises temperature) and latent heat (energy used for evaporation/transpiration), is a critical physical constraint for the distribution of energy at the surface. Validated in the Austrian cities of Innsbruck and Vienna, this regression-based CNN achieved an ensemble RMSE of approximately 2.22 K to 2.71 K, with over 80% of pixel errors falling within a ±3 K range. This demonstrates its capacity to effectively fill gaps caused by cloud cover and sensor revisit limitations by relying on the underlying physical drivers of surface temperature.

While the NRN [136] and regression-based CNNs [137] focus on feeding physical data into a CNN to guide the learning process, Liu et al. [138] proposed a physics guided CNN that explicitly integrates the ATC equation and a linear amplification module for ERA5 data as differentiable layers within the network. The proposed network does not just learn arbitrary patterns; it is constrained to learn specific physical parameters (mean temperature, amplitude, phase shift). Tested on Landsat data (30 m) at the Pennsylvania State University (PSU) site, this physics-guided framework achieved an RMSE of 3.44 K, significantly outperforming the standard CNN (RMSE 17.68 K), which failed to generalize due to temporal sparsity, and traditional ATC methods (RMSE 5.19 K) that could not capture daily extremes. When applied to GOES-16 data (2 km), the method achieved an RMSE of 2.67 K on held-out test data, demonstrating its ability to generate seamless daily temperature datasets across different spatial scales and weather conditions.

Another approach that utilizes physics-based loss functions to constrain the training process itself was proposed by Zhang et al. [139]. Trained on ERA5 reanalysis data, the architecture employs a two-stage design: a Masked Transformer Module with multi-head context attention captures long-range pixel dependencies and global structures, followed by a convolutional U-Net that refines local high-frequency details. To guide the model toward physically plausible solutions, it incorporates a weighted reconstruction loss that prioritizes missing regions and a novel gradient consistency regularization term, which forces the model to preserve thermal gradients and sharp physical boundaries (such as temperature fronts) rather than over-smoothing them. Once the model learned the reconstruction patterns from ERA5, it was then applied to real FengYun-3D (FY-3D) satellite data to fill orbital and cloud gaps. In a case study covering the Eastern Pacific and the East Coast of North America, the framework reconstructed surface temperature fields with a remarkable RMSE of 0.2000 K and a Structural Similarity Index of 0.9985, outperforming standard U-Net architectures. Crucially, these performance metrics characterize the model's ability to reconstruct the ERA5 dataset under artificial masking; however, its application to real FengYun-3D (FY-3D) satellite data—to fill actual orbital and cloud gaps—was evaluated qualitatively. While visual results demonstrate the framework's ability to generate seamless transitions, the study does not report a quantitative accuracy metric for the real satellite reconstruction, reflecting the persistent challenge of obtaining cloud-free ground truth for validation.

While the previously discussed frameworks rely heavily on CNN backbones, the Deep Ensemble Learning (DELAG) framework proposed by Liu et al. [140] represents a shift toward a two-stage design, in which an enhanced ATC is first solved using deep ensemble learning, followed by residual modeling with Gaussian Processes. The model explicitly incorporates physics by fitting an ATC for Landsat 8 and Landsat 9 with ERA5 reanalysis skin temperature included as a linear term. This allows the model to capture daily thermal fluctuations that a standard seasonal curve would miss, effectively amplifying the coarse ERA5 signal into fine-scale Landsat values. This method is distinct from classical machine learning ensembles because it relies on capturing multiple snapshots of model parameters from a single training trajectory to generate an ensemble, rather than training multiple independent models as is typical in classical approaches like bagging or boosting. By exploiting the non-convex loss landscape of the deep neural network, the framework collects these snapshots as the optimizer (Adam) fluctuates within a low-loss basin, allowing it to efficiently generate 200 model states for uncertainty quantification and the construction of 95% prediction intervals without the computational cost of training hundreds of separate networks. The study validates the reconstruction against near-surface air temperature for New York City, London, and Hong Kong, as in-situ LST sites were unavailable in these urban centers. The reported RMSE of 0.84–1.62 K under heavily cloudy conditions (¿80% cloud cover) and the provision of 95% confidence intervals demonstrate the method's ability to provide a rigorous, physics-anchored baseline for urban climate adaptation.

In summary, LST reconstruction has evolved from generic deep learning approaches toward specialized, physics-guided frameworks. Context-aware architectures, such as those utilizing non-local attention or Transformers, excel at repairing large spatial gaps by capturing global dependencies and multi-scale structures that standard convolutions miss. These models incorporate physical data by fusing satellite observations with coarse-resolution assimilation products, using attention mechanisms to map physics-based thermal baselines to fine-scale surface features. Other approaches achieve physical consistency by embedding the enhanced ATC directly into the model formulation or utilizing surface energy balance drivers to derive LST independently. Furthermore, the integration of deep ensembles has introduced a probabilistic dimension, allowing these frameworks to move beyond deterministic point estimates to robust uncertainty quantification.

However, while embedding physical equations like the enhanced ATC improves interpretability and consistency, it can also introduce model-form bias, potentially limiting the model's ability to capture anomalous thermal events that deviate from idealized physical assumptions. On the other hand, the heavy reliance on high-quality reanalysis inputs implies that the accuracy of many physics-guided models is

fundamentally constrained by the resolution and fidelity of the atmospheric data used to drive them. Addressing these limitations—particularly through improved validation strategies, hybrid physical formulations, and robust uncertainty-aware modeling—remains a key direction for future research.

The technical evolution of these methodologies, transitioning from foundational physical models to integrated deep learning architectures, is synthesized in Table VIII. This framework maps specific methodological categories to their corresponding thematic trends, providing a high-level perspective on the conceptual shifts and the strategic trade-offs currently defining the field of LST reconstruction.

IV. Discussion and Outlook

The reviewed studies highlight a range of methods for reconstructing LST, each with varying degrees of accuracy, geographic focus, and assumptions about data availability. Figure 13 provides a comprehensive overview of the reviewed methods.

The evolution of LST gap-filling techniques demonstrates that increased algorithmic complexity does not inherently guarantee superior performance. There is no universally optimal method. The most effective approach is highly contextual, requiring a balance between the desired precision, the specific characteristics of the study area, and the computational resources available. Key factors influencing model selection include spatial resolution and land cover heterogeneity. Meaning that, methods that excel at 1-km MODIS scales are more likely to struggle with the high spatial heterogeneity of 30-m Landsat data. This is evidenced by Guo et al. [141] who evaluated the performance of eight gap-filling methods for Landsat-7 and Landsat-8 LST data collected in 2016 across three regions in China: Shandong, Beijing, and Shaanxi. The authors concluded that the Enhanced ATC, which is a relatively simple model, was the optimal method among the eight tested. A surprising finding was that adding the ATC to existing methods creating hybrid versions like ATC+ESTARFM or ATC+LGBM did not necessarily improve statistical accuracy. The simple linear regression used by EATC was more adaptable to high-resolution residual prediction than the complex weighting algorithms used in ESTARFM or the machine learning used in LGBM.

A decision framework for selecting LST gap-filling strategy is established in Table IX.

A. Limitations

While many techniques show strong performance under ideal conditions—such as low cloud contamination and homogenous land cover—several key limitations emerge when evaluating them across different regions, temporal scales, and validation approaches.

1) Limited evaluation across diverse regions and time periods: Most reviewed methods are evaluated through specific case studies. A key limitation across methods is their performance variability depending on the region and dominant land cover, along with the restricted study period. For instance, the effectiveness of LST reconstruction using ATC-3DCNN was assessed primarily in Urban Beijing, China, using data from 2017 [110]. Other methods, such as the ubESTARFM data fusion model integrating Landsat and MODIS, have demonstrated reliable accuracy in forested regions of Australia (RMSE: 2.57 K) [76]. However, their applicability remains uncertain in areas with sparse vegetation, bare soil, deserts, and urban environments due to a lack of testing. Likewise, the HANTS model was evaluated using 2005 data from the Yangtze River Delta, a region characterized by agricultural land and forested mountains [51]. However, this model is restricted to simulating intra-annual variations in LST. The authors recommend applying the HANTS algorithm separately for each year, as LST in different years may exhibit different intra-annual variations.
2) Reliance on the quality of auxiliary data: Numerous methods depend on auxiliary data such as albedo, NDVI, EVI, and simulated LST, among others. However, spatial mismatches between datasets of varying resolutions are common. The accuracy of estimated LST is significantly influenced by both the resolution and precision of these auxiliary datasets, with potential inaccuracies arising from inherent uncertainties and the resampling of the auxiliary data.
3) Cloud cover and data gaps: Cloud contamination remains a major challenge for LST reconstruction, with high cloud cover often leading to reconstruction failures. The ability to reconstruct missing data hinges on identifying and leveraging correlations within the available data. When large gaps occur, there might be insufficient surrounding information to accurately determine these spatial or temporal relationships across the missing areas. Several studies have highlighted this limitation, noting that methods such as ATC-IDW fail when cloud cover exceeds 70% [72], emphasizing the difficulty of interpolating missing data in heavily clouded conditions. Likewise, DINEOF-CDF, a globally tested method, struggles with high uncertainties in persistently cloudy regions (RMSE: 4 – 7 K) [124] and requires further algorithmic refinements to improve performance.
4) Accuracy metrics and validation inconsistencies: One of the main challenges in comparing different methods is the inconsistent use of accuracy metrics. Some studies report RMSE (e.g., HANTS, MDINEOF), while others use MAE (e.g., SADFAT, ADTC, GraphProp). This makes direct comparisons difficult, as different metrics emphasize different aspects of model performance.
Additionally, the validation data themselves vary significantly. Some methods, such as MDINEOF and DINEOF-CDF, use simulated data (e.g., ERA5), while others like STRF and ubESTARFM use in-situ measurements. The lack of a standardized validation framework means that results may not be directly comparable. For example, Satellite-LSM, applied to Wuhan and Heihe River Basin, shows different performance levels depending on whether it is validated using in-situ data (RMSE: 2.66 – 4.36 K) or artificially masked pixels (RMSE: 0.97 – 1.26 K) [24].

TABLE VIII
THEMATIC TRENDS AND CONTRIBUTING METHODOLOGICAL CATEGORIES IN LST RECONSTRUCTION.

Thematic Trend	Contributing Categories	Synthesis of Insight & Perspective
Physical Consistency	• SEB-based • PGDL	Shift from modular energy balance snapshots to embedding physical laws (e.g., ATC/DTC) as differentiable network layers, reducing model-form bias.
Dynamic Resilience	• Multi-temporal • Hybrid ATC/DTC	Characterizing cumulative warming processes from sunrise rather than instantaneous transitions improves resilience to forcing data noise.
Global Scalability	• Data Assimilation • CDF Matching	Transitioning from local case studies to global monitoring via Kalman filtering of time-evolving ERA5 signals for all-weather consistency.
Uncertainty Quantification	• Deep Ensembles • Bayesian ML	Advancement from deterministic point estimates to generating 95% prediction intervals, essential for urban climate risk assessment.
Spatiotemporal Fidelity	• Non-local Attention • Graph Learning	Leveraging spectral similarity and global dependencies to repair large contiguous gaps that standard local convolutions fail to resolve.
Pragmatic Efficiency	• Classical ML • Simplified ATC	Evidence that algorithmic complexity does not guarantee accuracy; simple linear models often outperform complex hybrids in high-resolution residual prediction.

TABLE IX
DECISION FRAMEWORK FOR SELECTING LST GAP-FILLING STRATEGY

Scenario	Recommended Strategy	Rationale
Small isolated gaps	Spatial interpolation	Low computational cost
Periodic seasonal missing data	Temporal harmonic models	Captures annual cycle
Large contiguous cloud cover	Spatiotemporal or Fusion	Uses multi-date information
Persistent cloudy regions	TIR–PMW fusion	All-weather capability
Urban heterogeneity studies	TIR–TIR fusion or ML	Preserves fine spatial detail
Climate trend analysis	Physics-enhanced or hybrid	Ensures physical consistency
Global-scale application	DCT-PLS or scalable ML	Computational efficiency

5) Machine learning and deep learning considerations: Several machine learning approaches have shown promising results but remain sensitive to the extent of cloud cover and the accuracy of auxiliary data. Additionally, hyperparameter tuning remains a well-known challenge for deep learning methods. In the LSTM model, parameters are tuned based on trial and error, and the accuracy of reconstruction at a given time point depends on the availability and quality of preceding temporal data. In the ATC-3D-CNN model, it is not explicitly stated that a systematic or exhaustive trial and error process was conducted. However, it is likely based on common practices in deep learning with an element of trial and error involved. The effectiveness of the CNN in reconstructing remains influenced by the quality and availability of input data, including auxiliary data and the accuracy of preprocessing techniques such as interpolation.

B. Future Directions and Recommendations

Since 2014, the remote sensing community has increasingly shifted its attention to deep learning methods [142]. Techniques such as Fast Fourier Convolution (FFC) demonstrated promising performance in image-related tasks. However, despite its potential, it has not yet been extensively applied to the specific problem of gap-filling the cloud-contaminated LST. FFC is an advanced convolutional technique that performs convolution in the frequency domain using FFT, enabling efficient large receptive field operations. Unlike standard spatial-domain convolutions, which have a local receptive field restricted by the filter size, FFC operates in the frequency domain, allowing for efficient global feature extraction even in early network layers. Conceptually, FFC consists of two interconnected paths [143]:

1) The spatial (local) path, which applies standard convolutions to a subset of input feature channels, focusing on fine-grained local details with a limited receptive field.
2) The spectral (global) path, which transforms another subset of input features into the frequency domain using FFT, processes them to capture global patterns, and then applies the inverse FFT to return to the spatial domain.

The workflow of an FFC block is illustrated in Figure 14. An input X is divided into X_l and X_g, according to a predefined split factor α_{in}. The local path processes X_l, while the global path operates on X_g. After processing, the outputs of both paths are combined, enabling the network to effectively utilize both local details and global context.

Suvorov et al. [144] incorporated FFC into their resolution-robust Large Mask Inpainting (LaMa) model, demonstrating

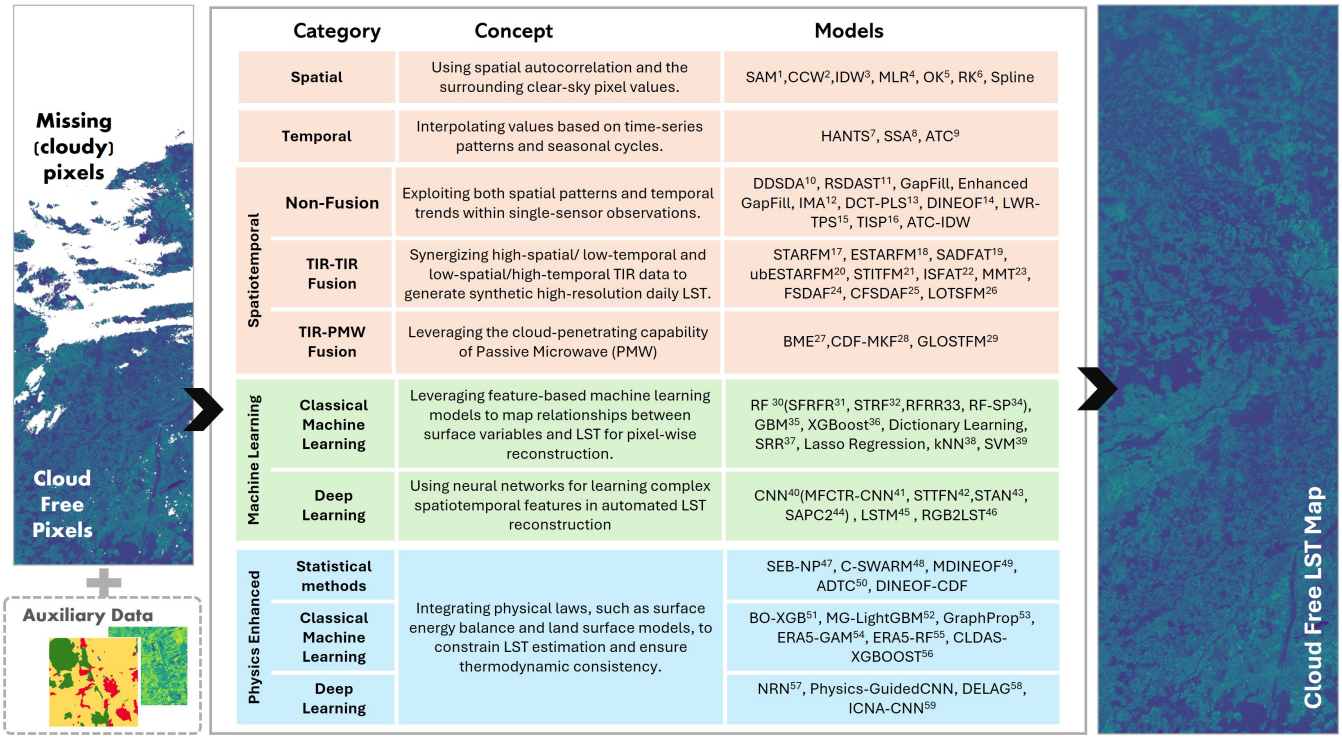

[1]**SAM:** Simple Arithmetic mean, [2]**CCW:** Correlation coefficient weighting, [3]**IDW:** Inverse distance weighting, [4]**MLR:** multiple linear regression, [5]**OK:** Ordinary kriging, [6]**RK:** Regression kriging, [7]**HANTS:** harmonic analysis of time series, [8]**SSA:** Singular spectrum decomposition, [9]**ATC:** Annual temperature cycle model, [10]**DDSDA:** Differential dynamic search distance algorithm, [11]**RSDAT** Remotely sensed daily land surface temperature reconstruction model [12]**IMA:** Interpolation of the mean anomalies, [13] **DCT-PLS:** Discrete cosine transform with penalized least square regression. [14]**DINEOF:** Data interpolating empirical orthogonal functions algorithm. [15]**LWR-TPS:** Hierarchical local weighted regression and thin plates spline. [16]**TISP:** Two-step Improved Similar Pixels Method, [17]**STRAFM** is the spatial and temporal adaptive reflectance fusion, [18]**ESTARFM:** Enhanced STARFM, [19]**SADFAT** is the spatiotemporal adaptive data fusion algorithm for temperature mapping, [20]**ubESTARFM**: unbiased ESTARFM, [21]**STITFM:** Spatio-Temporal Integrated Temperature Fusion Model, [22]**ISFAT:** Integrated spatiotemporal fusion algorithm, [23]**MMT:** Multisensor Multiresolution Technique , [24]**FSDAF:** Flexible spatiotemporal data fusion, [25]**CFSDAF:** Compressive FSDAF, [26]**LOTSFM:** Long time-series spatiotemporal fusion model, [27]**BME:** Bayesian Maximum Entropy, [28]**CDF-MKF:** Cumulative Distribution Function matching and Multiresolution Kalman Filtering, [29]**GLOSTFM:** Global Spatiotemporal Fusion Model, [30]**RF:** Random Forest, [31]**SFRFR:** Spatial feature-considered random forest regression [32]**STRF:**Spatial-Temporal RF, [33]**RFRR:** RF and Ridge Regression,[34]**RF-SP:** Hybrid RF-similar-pixel , [35]**GBM:** Gradient Boosting Machine, [36]**XGBoost:** Extreme gradient boosting, [37]**SRR:**Example-Based Super-Resolution Reconstruction, [38]**kNN:** k nearest neighbour, [39]**SVM:** Support Vector machines, [40]**CNN:** Convolutional neural network, [41]**MFCTR-CNN:** Multiscale Feature-Connected CNN, [42]**STTFN:** Spatiotemporal temperature fusion network, [43]**STAN:** Spatio-Temporal Attention Network, [44]**SAPC2:** Source Augmented Partial Convolution v2 model, [45]**LSTM** Long-short term memory, [46]**RGB2LST:** non-thermal RGB images to LST, [47]**SEB-NP:** Hybrid surface energy balance (SEB) and neighboring pixel (NP) analysis,[48]**C-SWAR:** Cloud-regulated Surface Warming Model, [49]**MDINEOF:** Multivariate data interpolating empirical orthogonal functions, [50]**ADTC:** Annual and diurnal temperature cycle - based framework, [51]**BO-XGB:** Bayesian Optimized XGBoost, [52]**MG-LightGBM:** Mechanism-Guided light gradient boosting machine, [53]**GraphProp:** Graph-based learning method, [54]**ERA5-GAM:** Generalized Additive model with ERA5 Reanalysis data as physical constraint, [55]**ERA5-RF:**RF with ERA5 Reanalysis data as physical constraint ,[56]**CLDAS-XGBOOST:** XGBOOST with Land Data Assimilation System (CLDAS) as physical linking variables, [57]**NRN:** Nonlocality-Reinforced Network, [58]**DELAG:** Deep Ensemble Learning, [59]**ICNA-CNN:** Regression based CNN fed with INCA meteorological data

Fig. 13. Overview of gap-filling techniques for reconstructing cloud-covered LST pixels

its effectiveness in capturing global contextual information. Bochow et al. [145] trained the LaMa model and successfully applied it to reconstruct several temperature datasets, including Berkeley Earth Surface Temperatures (BEST), HadCRUT4 observational data, CMIP5 historical surface temperatures, in addition to sea ice concentration. Expanding on this concept, Guo et al. [146] introduced a novel method named Cloud Perception Integrated Fast Fourier Convolutional Network (CP-FFCN), which integrates FFC into the U-net architecture for removing thin clouds from single remote sensing images. The proposed model outperforms U-Net with standard convolution on Landsat-8 images.

Despite these encouraging results, FFC-based methods have not yet been widely explored for the specific task of gap-filling cloud-contaminated LST products. Given the inherent advantage of FFC in capturing global spatial context, this represents a promising direction for advancing LST reconstruction methodologies.

To further improve LST gap-filling and reconstruction, future research should address the following:

1) Standardized evaluation: a consistent accuracy metrics (RMSE, MAE, R^2) and validation datasets over diverse geographic regions will enhance the comparability of methods. Expanding validation to diverse landscapes, including deserts, mountains, and coastal regions, will improve model generalizability.
2) Enhancing auxiliary data: Given that numerous methods rely on auxiliary datasets, improving the spatial and temporal resolution of these inputs will directly enhance reconstruction accuracy. Research could explore more accurate resampling techniques that minimize distortion when matching the resolution of the primary LST data to auxiliary data, reducing inaccuracies from spatial or temporal mismatches. A more accurate resampling technique can further improve overall accuracy by employing advanced mathematical or statistical methods. Furthermore, adaptive resampling strategies, which account for the underlying physical processes in each dataset, could be explored to enhance performance. Adaptive resampling would dynamically adjust resampling methods based on the characteristics or needs of the data, therby enhancing the overall process where required.

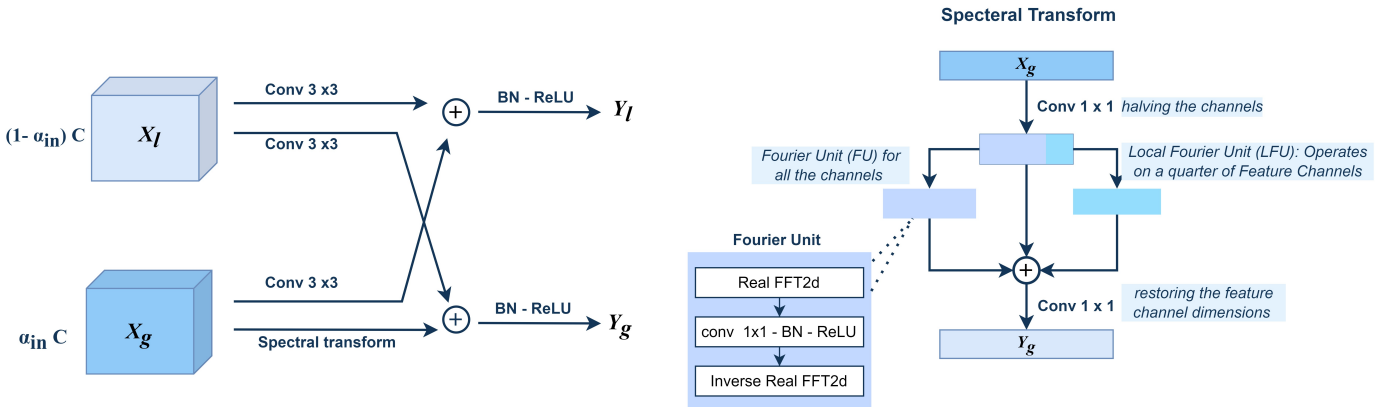

Fig. 14. FFC block structure

3) Integration of deep learning for improved cloud handling: Existing techniques remain sensitive to cloud cover extent. While deep learning has shown promise, further exploration of advanced architectures is needed. For instance, Fast Fourier Convolution, which enables an image-wide receptive field from early training stages, could help mitigate inaccuracies caused by large data gaps. As a notable application of Fast Fourier Convolution, LaMa demonstrates its effectiveness in addressing data gaps and deserves further exploration.

V. Conclusion

This paper provides a comprehensive review of state-of-the-art methods for reconstructing LST data affected by cloud contamination in remote sensing imagery. The review highlights both the advances achieved and the challenges that remain, offering valuable insights for future research focused on improving the accuracy, robustness, generalizability, and applicability of LST recovery methods under cloud-covered conditions.

The reviewed methods were broadly categorized into two main groups: rule-based approaches and data-driven approaches. Rule-based methods reconstruct missing LST values by leveraging spatial and temporal correlations, physical principles, and complementary auxiliary datasets. In contrast, data-driven methods, particularly those based on machine learning and deep learning, model the complex nonlinear relationships inherent in LST dynamics to predict and reconstruct missing information.

More than 50 representative methods were reviewed within these categories. While each method demonstrated promising results, several limitations were consistently noted across the methods. These included regional specificity, reduced performance under conditions of persistent or extensive cloud cover, and a strong dependence on the availability and quality of auxiliary data. Additionally, the lack of standardized accuracy metrics across studies complicates direct comparisons of the methods' effectiveness.

Finally, this study outlines directions for future research by highlighting unresolved challenges and identifying potential methods that can be adapted for gap-filling of cloud-contaminated LST data.

VI. Conflict of Interest

The authors declare no conflicts of interest.

Acknowledgements

The work presented in this paper was supported by TUM International Graduate School of Science and Engineering (IGSSE) within the scope of the Innovation Network EarthCare.

References

[1] P. Dash, F.-M. Göttsche, F.-S. Olesen, and H. Fischer, "Land surface temperature and emissivity estimation from passive sensor data: Theory and practice-current trends," *International Journal of Remote Sensing*, vol. 23, no. 13, pp. 2563–2594, 2002. [Online]. Available: https://doi.org/10.1080/01431160110115041

[2] W. Tang, J. Zhou, J. Ma, Z. Wang, L. Ding, X. Zhang, and X. Zhang, "Trims lst: a daily 1 km all-weather land surface temperature dataset for china's landmass and surrounding areas (2000–2022)," *Earth System Science Data*, vol. 16, no. 1, pp. 387–419, 2024. [Online]. Available: https://essd.copernicus.org/articles/16/387/2024/

[3] Z.-L. Li, H. Wu, S.-B. Duan, W. Zhao, H. Ren, X. Liu, P. Leng, R. Tang, X. Ye, J. Zhu, Y. Sun, M. Si, M. Liu, J. Li, X. Zhang, G. Shang, B.-H. Tang, G. Yan, and C. Zhou, "Satellite remote sensing of global land surface temperature: Definition, methods, products, and applications," *Reviews of Geophysics*, vol. 61, no. 1, p. e2022RG000777, 2023, e2022RG000777 2022RG000777. [Online]. Available: https://agupubs.onlinelibrary.wiley.com/doi/abs/10.1029/2022RG000777

[4] B. Candy, R. W. Saunders, D. Ghent, and C. E. Bulgin, "The impact of satellite-derived land surface temperatures on numerical weather prediction analyses and forecasts," *Journal of Geophysical Research: Atmospheres*, vol. 122, no. 18, pp. 9783–9802, 2017. [Online]. Available: https://agupubs.onlinelibrary.wiley.com/doi/abs/10.1002/2016JD026417

[5] M. Z. Sassi, N. Fourrié, V. Guidard, and C. Birman, "Use of infrared satellite observations for the surface temperature retrieval over land in a nwp context," *Remote Sensing*, vol. 11, no. 20, 2019. [Online]. Available: https://www.mdpi.com/2072-4292/11/20/2371

[6] Y. Ren, X. Gao, Y. Liu, Z. Li, and W. Liu, "Assessment and improvement of regcm 4.6 coupled with clm4.5 in simulation of land surface temperature in mainland china," *Theoretical and Applied Climatology*, vol. 153, no. 3, 2023. [Online]. Available: https://doi.org/10.1007/s00704-023-04487-0

[7] F. Silvestro, S. Gabellani, F. Delogu, R. Rudari, and G. Boni, "Exploiting remote sensing land surface temperature in distributed hydrological modelling: the example of the continuum model," *Hydrology and Earth System Sciences*, vol. 17, no. 1, pp. 39–62, 2013. [Online]. Available: https://hess.copernicus.org/articles/17/39/2013/

[8] J. Muro, A. Strauch, S. Heinemann, S. Steinbach, F. Thonfeld, B. Waske, and B. Diekkrüger, "Land surface temperature trends as indicator of land use changes in wetlands," *International Journal of Applied Earth Observation and Geoinformation*, vol. 70, pp. 62–71, 2018. [Online]. Available: https://www.sciencedirect.com/science/article/pii/S0303243418301144

[9] R. Fernandes, V. Nascimento, M. Freitas, and J. Ometto, "Local climate zones to identify surface urban heat islands: A systematic review," *Remote Sensing*, vol. 15, 2023. [Online]. Available: https://www.mdpi.com/2072-4292/15/4/884

[10] P. Reiners, J. Sobrino, and C. Kuenzer, "Satellite-derived land surface temperature dynamics in the context of global change—a review," *Remote Sensing*, vol. 15, no. 7, 2023. [Online]. Available: https://www.mdpi.com/2072-4292/15/7/1857

[11] X. Li, J. Xiao, J. B. Fisher, and D. D. Baldocchi, "Ecostress estimates gross primary production with fine spatial resolution for different times of day from the international space station," *Remote Sensing of Environment*, vol. 258, p. 112360, 2021. [Online]. Available: https://www.sciencedirect.com/science/article/pii/S003442572100078X

[12] S. Li, J. Wang, D. Li, Z. Ran, and B. Yang, "Evaluation of landsat 8-like land surface temperature by fusing landsat 8 and modis land surface temperature product," *Processes*, vol. 9, 2021. [Online]. Available: https://www.mdpi.com/2227-9717/9/12/2262

[13] Y. Mo, Y. Xu, H. Chen, and S. Zhu, "A review of reconstructing remotely sensed land surface temperature under cloudy conditions," *Remote Sensing*, vol. 13, 2021. [Online]. Available: https://www.mdpi.com/2072-4292/13/14/2838

[14] P. Wu, Z. Yin, C. Zeng, S.-B. Duan, F.-M. Göttsche, X. Ma, X. Li, H. Yang, and H. Shen, "Spatially continuous and high-resolution land surface temperature product generation: A review of reconstruction and spatiotemporal fusion techniques," *IEEE Geoscience and Remote Sensing Magazine*, vol. 9, no. 3, pp. 112–137, 2021.

[15] L. Wanner, M. Calaf, and M. Mauder, "Incorporating the effect of heterogeneous surface heating into a semi-empirical model of the surface energy balance closure," *PLOS ONE*, vol. 17, no. 6, pp. 1–21, 06 2022. [Online]. Available: https://doi.org/10.1371/journal.pone.0268097

[16] M. Mauder, T. Foken, and J. Cuxart, "Surface-energy-balance closure over land: A review," *Boundary-Layer Meteorology*, 2020.

[17] J. Cuxart, L. Conangla, and M. A. Jiménez, "Evaluation of the surface energy budget equation with experimental data and the ecmwf model in the ebro valley," *Journal of Geophysical Research: Atmospheres*, vol. 120, no. 3, pp. 1008–1022, 2015. [Online]. Available: https://agupubs.onlinelibrary.wiley.com/doi/abs/10.1002/2014JD022296

[18] Z. Su, "The surface energy balance system (sebs) for estimation of turbulent heat fluxes," *Hydrology and Earth System Sciences*, vol. 6, no. 1, pp. 85–100, 2002. [Online]. Available: https://hess.copernicus.org/articles/6/85/2002/

[19] P. Viterbo and A. C. Beljaars, "An improved land surface parameterization scheme in the ecmwf model and its validation," *Journal of climate*, vol. 8, no. 11, pp. 2716–2748, 1995.

[20] R. A. Fisher and C. D. Koven, "Perspectives on the future of land surface models and the challenges of representing complex terrestrial systems," *Journal of Advances in Modeling Earth Systems*, vol. 12, no. 4, p. e2018MS001453, 2020, e2018MS001453 2018MS001453. [Online]. Available: https://agupubs.onlinelibrary.wiley.com/doi/abs/10.1029/2018MS001453

[21] W. Y. Lee, H.-J. Gim, and S. K. Park, "Parameterizations of snow cover, snow albedo and snow density in land surface models: A comparative review," *Asia-Pacific Journal of Atmospheric Sciences*, vol. 60, 2024.

[22] J. Koch, A. Siemann, S. Stisen, and J. Sheffield, "Spatial validation of large-scale land surface models against monthly land surface temperature patterns using innovative performance metrics," *Journal of Geophysical Research: Atmospheres*, vol. 121, no. 10, pp. 5430–5452, 2016. [Online]. Available: https://agupubs.onlinelibrary.wiley.com/doi/abs/10.1002/2015JD024482

[23] D. Ghent, J. Kaduk, J. Remedios, J. Ardö, and H. Balzter, "Assimilation of land surface temperature into the land surface model jules with an ensemble kalman filter," *Journal of Geophysical Research: Atmospheres*, vol. 115, no. D19, 2010. [Online]. Available: https://agupubs.onlinelibrary.wiley.com/doi/abs/10.1029/2010JD014392

[24] J. Ma, H. Shen, P. Wu, J. Wu, M. Gao, and C. Meng, "Generating gapless land surface temperature with a high spatio-temporal resolution by fusing multi-source satellite-observed and model-simulated data," *Remote Sensing of Environment*, vol. 278, p. 113083, 2022. [Online]. Available: https://www.sciencedirect.com/science/article/pii/S0034425722001973

[25] B. Dumitrescu and P. Irofti, *Dictionary Learning Algorithms and Applications*. Springer International Publishing, 2018.

[26] M. Lewicki and T. Sejnowski, "Learning overcomplete representations," *Neural Computation*, vol. 12, pp. 337–365, 2 2000.

[27] H. A. Salman, A. Kalakech, and A. Steiti, "Random forest algorithm overview," *Babylonian Journal of Machine Learning*, vol. 2024, pp. 69–79, 6 2024.

[28] R. Guo, Z. Zhao, T. Wang, G. Liu, J. Zhao, and D. Gao, "Degradation state recognition of piston pump based on iceemdan and xgboost," *Applied Sciences*, vol. 10, p. 6593, 2 2020.

[29] M. Valizadeh and S. J. Wolff, "Convolutional neural network applications in additive manufacturing: A review," *Advances in Industrial and Manufacturing Engineering*, vol. 4, p. 100072, 2022. [Online]. Available: https://www.sciencedirect.com/science/article/pii/S2666912922000046

[30] L. Alzubaidi, J. Zhang, A. J. Humaidi, A. Al-Dujaili, Y. Duan, O. Al-Shamma, J. Santamaría, M. A. Fadhel, M. Al-Amidie, and L. Farhan, "Review of deep learning: concepts, cnn architectures, challenges, applications, future directions," *Journal of Big Data*, vol. 8, 12 2021.

[31] Y. LeCun, B. Boser, J. S. Denker, D. Henderson, R. E. Howard, W. Hubbard, and L. D. Jackel, "Backpropagation applied to handwritten zip code recognition," *Neural Computation*, vol. 1, pp. 541–551, 2 1989. [Online]. Available: https://doi.org/10.1162/neco.1989.1.4.541

[32] A. Krizhevsky, I. Sutskever, and G. E. Hinton, "Imagenet classification with deep convolutional neural networks," F. Pereira, C. J. Burges, L. Bottou, and K. Q. Weinberger, Eds., vol. 25. Curran Associates, Inc., 2012. [Online]. Available: https://proceedings.neurips.cc/paper_files/paper/2012/file/c399862d3b9d6b76c8436e924a68c45b-Paper.pdf

[33] K. Simonyan and A. Zisserman, "Very deep convolutional networks for large-scale image recognition," *CoRR*, vol. abs/1409.1556, 2014. [Online]. Available: https://api.semanticscholar.org/CorpusID:14124313

[34] K. He, X. Zhang, S. Ren, and J. Sun, "Deep residual learning for image recognition," *2016 IEEE Conference on Computer Vision and Pattern Recognition (CVPR)*, pp. 770–778, 2015. [Online]. Available: https://api.semanticscholar.org/CorpusID:206594692

[35] C. Szegedy, W. Liu, Y. Jia, P. Sermanet, S. Reed, D. Anguelov, D. Erhan, V. Vanhoucke, and A. Rabinovich, "Going deeper with convolutions," 2015, pp. 1–9.

[36] Philipp, B. T. R. Olaf, and Fischer, "U-net: Convolutional networks for biomedical image segmentation," Joachim, W. W. M., F. A. F. N. Nassir, and Hornegger, Eds. Springer International Publishing, 2015, pp. 234–241.

[37] S. M. Al-Selwi, M. F. Hassan, S. J. Abdulkadir, A. Muneer, E. H. Sumiea, A. Alqushaibi, and M. G. Ragab, "Rnn-lstm: From applications to modeling techniques and beyond—systematic review," *Journal of King Saud University - Computer and Information Sciences*, vol. 36, 6 2024.

[38] J. Sen and S. Mehtab, "Long-and-short-term memory (lstm) networks architectures and applications in stock price prediction," *Emerging Computing Paradigms*, pp. 143–160, 2022. [Online]. Available: https://onlinelibrary.wiley.com/doi/abs/10.1002/9781119813439.ch8

[39] G. V. Houdt, C. Mosquera, and G. Nápoles, "A review on the long short-term memory model," *Artificial Intelligence Review*, vol. 53, pp. 5929–5955, 12 2020.

[40] J. Gui, Z. Sun, Y. Wen, D. Tao, and J. Ye, "A review on generative adversarial networks: Algorithms, theory, and applications," *IEEE Transactions on Knowledge and Data Engineering*, vol. 35, pp. 3313–3332, 2023.

[41] A. Radford, L. Metz, and S. Chintala, "Unsupervised representation learning with deep convolutional generative adversarial networks," *CoRR*, vol. abs/1511.06434, 2015. [Online]. Available: https://api.semanticscholar.org/CorpusID:11758569

[42] M. Mirza and S. Osindero, "Conditional generative adversarial nets," *ArXiv*, vol. abs/1411.1784, 2014. [Online]. Available: https://api.semanticscholar.org/CorpusID:12803511

[43] A. Kuznetsov and M. Gashnikov, "Remote sensing image inpainting with generative adversarial networks," 2020, pp. 1–6.

[44] F. W. Chen and C. W. Liu, "Estimation of the spatial rainfall distribution using inverse distance weighting (idw) in the middle of taiwan," *Paddy and Water Environment*, vol. 10, pp. 209–222, 9 2012. [Online]. Available: https://link.springer.com/article/10.1007/s10333-012-0319-1

[45] N. Lam, "Spatial interpolation methods: A review," *Cartography and Geographic Information Science - CARTOGR GEOGR INF SCI*, vol. 10, pp. 129–150, 11 1983.

[46] X. Zhu, D. Liu, and J. Chen, "A new geostatistical approach for filling gaps in landsat etm+ slc-off images," *Remote Sensing*

of Environment, vol. 124, pp. 49–60, 2012. [Online]. Available: https://www.sciencedirect.com/science/article/pii/S0034425712001952

[47] T. Hengl, G. B. Heuvelink, and D. G. Rossiter, "About regression-kriging: From equations to case studies," *Computers & Geosciences*, vol. 33, no. 10, pp. 1301–1315, 2007, spatial Analysis. [Online]. Available: https://www.sciencedirect.com/science/article/pii/S0098300407001008

[48] L. Ke, X. Ding, and C. Song, "Reconstruction of time-series modis lst in central qinghai-tibet plateau using geostatistical approach," *IEEE Geoscience and Remote Sensing Letters*, vol. 10, pp. 1602–1606, 2013.

[49] P. Wu, Z. Yin, H. Yang, Y. Wu, and X. Ma, "Reconstructing geostationary satellite land surface temperature imagery based on a multiscale feature connected convolutional neural network," *Remote Sensing*, vol. 11, 2019. [Online]. Available: https://www.mdpi.com/2072-4292/11/3/300

[50] S. Azzali and M. Menenti, *Fourier analysis of temporal NDVI in the Southern African and American continents*. Board of Remote Sensing (BCRS), 1996.

[51] Y. Xu and Y. Shen, "Reconstruction of the land surface temperature time series using harmonic analysis," *Computers & Geosciences*, vol. 61, pp. 126–132, 2013. [Online]. Available: https://www.sciencedirect.com/science/article/pii/S0098300413002367

[52] F. Arabi Aliabad, E. Ghaderpour, A. Mazidi, and F. Houshmandzade, "Gap-filling of land surface temperature in arid regions by combining landsat 8 and 9 imageries," *Environmental Research Communications*, vol. 6, no. 10, p. 105037, oct 2024. [Online]. Available: https://doi.org/10.1088/2515-7620/ad898e

[53] H. R. Ghafarian Malamiri, I. Rousta, H. Olafsson, H. Zare, and H. Zhang, "Gap-filling of modis time series land surface temperature (lst) products using singular spectrum analysis (ssa)," *Atmosphere*, vol. 9, no. 9, 2018. [Online]. Available: https://www.mdpi.com/2073-4433/9/9/334

[54] B. Bechtel, "Robustness of annual cycle parameters to characterize the urban thermal landscapes," *IEEE Geoscience and Remote Sensing Letters*, vol. 9, pp. 876–880, 2012.

[55] Z. Liu, W. Zhan, J. Lai, F. Hong, J. Quan, B. Bechtel, F. Huang, and Z. Zou, "Balancing prediction accuracy and generalization ability: A hybrid framework for modelling the annual dynamics of satellite-derived land surface temperatures," *ISPRS Journal of Photogrammetry and Remote Sensing*, vol. 151, pp. 189–206, 2019. [Online]. Available: https://www.sciencedirect.com/science/article/pii/S0924271619300826

[56] Z. Zou, W. Zhan, Z. Liu, B. Bechtel, L. Gao, F. Hong, F. Huang, and J. Lai, "Enhanced modeling of annual temperature cycles with temporally discrete remotely sensed thermal observations," *Remote Sensing*, vol. 10, no. 4, 2018. [Online]. Available: https://www.mdpi.com/2072-4292/10/4/650

[57] N. Siabi, S. H. Sanaeinejad, and B. Ghahraman, "Effective method for filling gaps in time series of environmental remote sensing data: An example on evapotranspiration and land surface temperature images," *Computers and Electronics in Agriculture*, vol. 193, p. 106619, 2022. [Online]. Available: https://www.sciencedirect.com/science/article/pii/S0168169921006360

[58] L. Sun, Z. Chen, F. Gao, M. Anderson, L. Song, L. Wang, B. Hu, and Y. Yang, "Reconstructing daily clear-sky land surface temperature for cloudy regions from modis data," *Computers & Geosciences*, vol. 105, pp. 10–20, 2017. [Online]. Available: https://www.sciencedirect.com/science/article/pii/S0098300416308135

[59] T. Zhang, Y. Zhou, Z. Zhu, X. Li, and G. R. Asrar, "A global seamless 1 km resolution daily land surface temperature dataset (2003–2020)," *Earth System Science Data*, vol. 14, no. 2, pp. 651–664, 2022. [Online]. Available: https://essd.copernicus.org/articles/14/651/2022/

[60] F. Gerber, R. de Jong, M. E. Schaepman, G. Schaepman-Strub, and R. Furrer, "Predicting missing values in spatio-temporal remote sensing data," *IEEE Transactions on Geoscience and Remote Sensing*, vol. 56, no. 5, pp. 2841–2853, 2018.

[61] A. F. Militino, M. D. Ugarte, U. Pérez-Goya, and M. G. Genton, "Interpolation of the mean anomalies for cloud filling in land surface temperature and normalized difference vegetation index," *IEEE Transactions on Geoscience and Remote Sensing*, vol. 57, no. 8, pp. 6068–6078, 2019.

[62] X. Li, Y. Zhou, G. R. Asrar, and Z. Zhu, "Creating a seamless 1km resolution daily land surface temperature dataset for urban and surrounding areas in the conterminous united states," *Remote Sensing of Environment*, vol. 206, pp. 84–97, 2018. [Online]. Available: https://www.sciencedirect.com/science/article/pii/S0034425717305850

[63] D. Garcia, "Robust smoothing of gridded data in one and higher dimensions with missing values," *Computational Statistics & Data Analysis*, vol. 54, no. 4, pp. 1167–1178, 2010. [Online]. Available: https://www.sciencedirect.com/science/article/pii/S0167947309003491

[64] H. T. Pham, S. Kim, L. Marshall, and F. Johnson, "Using 3d robust smoothing to fill land surface temperature gaps at the continental scale," *International Journal of Applied Earth Observation and Geoinformation*, vol. 82, p. 101879, 2019. [Online]. Available: https://www.sciencedirect.com/science/article/pii/S0303243419300339

[65] H. Liu, N. Lu, H. Jiang, J. Qin, and L. Yao, "Filling gaps of monthly terra/modis daytime land surface temperature using discrete cosine transform method," *Remote Sensing*, vol. 12, no. 3, 2020. [Online]. Available: https://www.mdpi.com/2072-4292/12/3/361

[66] W. Zhou, B. Peng, and J. Shi, "Reconstructing spatial–temporal continuous modis land surface temperature using the dineof method," *Journal of Applied Remote Sensing*, vol. 11, p. 46016, 2017. [Online]. Available: https://doi.org/10.1117/1.JRS.11.046016

[67] J. M. Beckers and M. Rixen, "Eof calculations and data filling from incomplete oceanographic datasets," *Journal of Atmospheric and Oceanic Technology*, vol. 20, pp. 1839 – 1856, 2003. [Online]. Available: https://journals.ametsoc.org/view/journals/atot/20/12/1520-0426_2003_020_1839_ecadff_2_0_co_2.xml

[68] National Center for Atmospheric Research Staff (Eds), "The climate data guide: Empirical orthogonal function (eof) analysis and rotated eof analysis," 7 2013. [Online]. Available: https://climatedataguide.ucar.edu/climate-data-tools-and-analysis/empirical-orthogonal-function-eof-analysis-and-rotated-eof-analysis

[69] A. ALVERA-AZCÁRATE, A. BARTH, D. SIRJACOBS, F. LENARTZ, and J. M. BECKERS, "Data interpolating empirical orthogonal functions (dineof): a tool for geophysical data analyses," *Mediterranean Marine Science*, vol. 12, pp. 5–11, 3 2011. [Online]. Available: https://ejournals.epublishing.ekt.gr/index.php/hcmr-med-mar-sc/article/view/12037

[70] M. Metz, V. Andreo, and M. Neteler, "A new fully gap-free time series of land surface temperature from modis lst data," *Remote Sensing*, vol. 9, no. 12, 2017. [Online]. Available: https://www.mdpi.com/2072-4292/9/12/1333

[71] J. Tan, T. Che, J. Wang, J. Liang, Y. Zhang, and Z. Ren, "Reconstruction of the daily modis land surface temperature product using the two-step improved similar pixels method," *Remote Sensing*, vol. 13, no. 9, 2021. [Online]. Available: https://www.mdpi.com/2072-4292/13/9/1671

[72] X. Zhu, S.-B. Duan, Z.-L. Li, P. Wu, H. Wu, W. Zhao, and Y. Qian, "Reconstruction of land surface temperature under cloudy conditions from landsat 8 data using annual temperature cycle model," *Remote Sensing of Environment*, vol. 281, p. 113261, 2022. [Online]. Available: https://www.sciencedirect.com/science/article/pii/S0034425722003674

[73] F. Gao, J. Masek, M. Schwaller, and F. Hall, "On the blending of the landsat and modis surface reflectance: predicting daily landsat surface reflectance," *IEEE Transactions on Geoscience and Remote Sensing*, vol. 44, pp. 2207–2218, 2006.

[74] X. Zhu, J. Chen, F. Gao, X. Chen, and J. G. Masek, "An enhanced spatial and temporal adaptive reflectance fusion model for complex heterogeneous regions," *Remote Sensing of Environment*, vol. 114, pp. 2610–2623, 11 2010.

[75] Q. Weng, P. Fu, and F. Gao, "Generating daily land surface temperature at landsat resolution by fusing landsat and modis data," *Remote Sensing of Environment*, vol. 145, pp. 55–67, 2014. [Online]. Available: https://www.sciencedirect.com/science/article/pii/S0034425714000479

[76] Y. Yu, L. J. Renzullo, T. R. McVicar, B. P. Malone, and S. Tian, "Generating daily 100 m resolution land surface temperature estimates continentally using an unbiased spatiotemporal fusion approach," *Remote Sensing of Environment*, vol. 297, p. 113784, 2023. [Online]. Available: https://www.sciencedirect.com/science/article/pii/S0034425723003358

[77] P. Wu, H. Shen, L. Zhang, and F.-M. Göttsche, "Integrated fusion of multi-scale polar-orbiting and geostationary satellite observations for the mapping of high spatial and temporal resolution land surface temperature," *Remote Sensing of Environment*, vol. 156, pp. 169–181, 2015. [Online]. Available: https://www.sciencedirect.com/science/article/pii/S0034425714003563

[78] I. A. Adeniran, M. Nazeer, M. S. Wong, R. Zhu, J. Yang, and P.-W. Chan, "Improved fusion model for generating hourly fine scale land surface temperature data under all-weather condition," *International Journal of Applied Earth Observation and Geoinformation*, vol. 131, p. 103981, 2024. [Online]. Available: https://www.sciencedirect.com/science/article/pii/S1569843224003352

[79] B. Zhukov, D. Oertel, F. Lanzl, and G. Reinhackel, "Unmixing-based multisensor multiresolution image fusion," *IEEE Transactions*

on Geoscience and Remote Sensing, vol. 37, no. 3, pp. 1212–1226, 1999.

[80] X. Zhu, E. H. Helmer, F. Gao, D. Liu, J. Chen, and M. A. Lefsky, "A flexible spatiotemporal method for fusing satellite images with different resolutions," *Remote Sensing of Environment*, vol. 172, pp. 165–177, 2016. [Online]. Available: https://www.sciencedirect.com/science/article/pii/S0034425715302042

[81] C. Shi, N. Wang, Q. Zhang, Z. Liu, and X. Zhu, "A comprehensive flexible spatiotemporal data fusion method (cfsdaf) for generating high spatiotemporal resolution land surface temperature in urban area," *IEEE Journal of Selected Topics in Applied Earth Observations and Remote Sensing*, vol. 15, pp. 9885–9899, 2022.

[82] Y. Li, H. Wu, Z.-L. Li, S. Duan, and L. Ni, "Evaluation of spatiotemporal fusion models in land surface temperature using polar-orbiting and geostationary satellite data," in *IGARSS 2020 - 2020 IEEE International Geoscience and Remote Sensing Symposium*, 2020, pp. 236–239.

[83] S. Chen, L. Zhang, X. Hu, Q. Meng, J. Qian, and J. Gao, "A spatiotemporal fusion model of land surface temperature based on pixel long time-series regression: Expanding inputs for efficient generation of robust fused results," *Remote Sensing*, vol. 15, no. 21, 2023. [Online]. Available: https://www.mdpi.com/2072-4292/15/21/5211

[84] R. Yao, L. Wang, X. Huang, L. Sun, R. Chen, X. Wu, W. Zhang, and Z. Niu, "A robust method for filling the gaps in modis and viirs land surface temperature data," *IEEE Transactions on Geoscience and Remote Sensing*, vol. 59, no. 12, pp. 10 738–10 752, 2021.

[85] S.-B. Duan, Y. Lian, E. Zhao, H. Chen, W. Han, and Z. Wu, "A novel approach to all-weather lst estimation using xgboost model and multisource data," *IEEE Transactions on Geoscience and Remote Sensing*, vol. 61, pp. 1–14, 2023.

[86] S.-B. Duan, Z.-L. Li, and P. Leng, "A framework for the retrieval of all-weather land surface temperature at a high spatial resolution from polar-orbiting thermal infrared and passive microwave data," *Remote Sensing of Environment*, vol. 195, pp. 107–117, 2017. [Online]. Available: https://www.sciencedirect.com/science/article/pii/S003442571730158X

[87] X. Kou, L. Jiang, Y. Bo, S. Yan, and L. Chai, "Estimation of land surface temperature through blending modis and amsr-e data with the bayesian maximum entropy method," *Remote Sensing*, vol. 8, no. 2, 2016. [Online]. Available: https://www.mdpi.com/2072-4292/8/2/105

[88] S. Xu, J. Cheng, and Q. Zhang, "Reconstructing all-weather land surface temperature using the bayesian maximum entropy method over the tibetan plateau and heihe river basin," *IEEE Journal of Selected Topics in Applied Earth Observations and Remote Sensing*, vol. 12, no. 9, pp. 3307–3316, 2019.

[89] S. Xu and J. Cheng, "A new land surface temperature fusion strategy based on cumulative distribution function matching and multiresolution kalman filtering," *Remote Sensing of Environment*, vol. 254, p. 112256, 2021. [Online]. Available: https://www.sciencedirect.com/science/article/pii/S0034425720306295

[90] T. P. F. Dowling, P. Song, M. C. D. Jong, L. Merbold, M. J. Wooster, J. Huang, and Y. Zhang, "An improved cloud gap-filling method for longwave infrared land surface temperatures through introducing passive microwave techniques," *Remote Sensing*, vol. 13, no. 17, 2021. [Online]. Available: https://www.mdpi.com/2072-4292/13/17/3522

[91] Q. Meng, S. Chen, L. Zhang, X. Zhu, Y. Zhang, and P. M. Atkinson, "Glostfm: A global spatiotemporal fusion model integrating multi-source satellite observations to enhance land surface temperature resolution," *Remote Sensing of Environment*, vol. 319, p. 114640, 2025. [Online]. Available: https://www.sciencedirect.com/science/article/pii/S0034425725000446

[92] I. Buo, V. Sagris, and J. Jaagus, "Gap-filling satellite land surface temperature over heatwave periods with machine learning," *IEEE Geoscience and Remote Sensing Letters*, vol. 19, pp. 1–5, 2022.

[93] Z. Wu, H. Teng, H. Chen, L. Han, and L. Chen, "Reconstruction of gap-free land surface temperature at a 100 m spatial resolution from multidimensional data: A case in wuhan, china," *Sensors*, vol. 23, 1 2023.

[94] Q. Wang, Y. Tang, X. Tong, and P. M. Atkinson, "Filling gaps in cloudy landsat lst product by spatial-temporal fusion of multi-scale data," *Remote Sensing of Environment*, vol. 306, p. 114142, 2024. [Online]. Available: https://www.sciencedirect.com/science/article/pii/S0034425724001536

[95] T. Chongtaku, A. Taparugssanagorn, H. Miyazaki, and T. W. Tsusaka, "Integrating remote sensing and ground-based data for enhanced spatial–temporal analysis of heatwaves: A machine learning approach," *Applied Sciences*, vol. 14, no. 10, 2024. [Online]. Available: https://www.mdpi.com/2076-3417/14/10/3969

[96] D. Chen, Q. Zhuang, L. Zhu, W. Zhang, and T. Sun, "Generating daily gap-free modis land surface temperature using the random forest model and similar pixels method," *IEEE Access*, vol. 11, pp. 103 274–103 287, 2023.

[97] X. Liu, W. Zhu, Q. Zhuang, T. Sun, and Z. Chen, "Generating 1 km seamless land surface temperature from china fy3c satellite data using machine learning," *Applied Sciences*, vol. 15, no. 11, 2025. [Online]. Available: https://www.mdpi.com/2076-3417/15/11/6202

[98] Y. Tang, Y. Zhao, Y. Sun, S. Ren, and Z. Li, "Seamless reconstruction of modis land surface temperature via multi-source data fusion and multi-stage optimization," *Remote Sensing*, vol. 17, no. 19, 2025. [Online]. Available: https://www.mdpi.com/2072-4292/17/19/3374

[99] J. Li, H. Yang, W. Chen, C. Li, and G. Yang, "Generating spatiotemporal seamless data of clear-sky land surface temperature using synthetic aperture radar, digital elevation mode, and machine learning over vegetation areas," *Journal of Remote Sensing*, vol. 4, p. 0071, 2024. [Online]. Available: https://spj.science.org/doi/abs/10.34133/remotesensing.0071

[100] X. Li, H. Shen, L. Zhang, H. Zhang, Q. Yuan, and G. Yang, "Recovering quantitative remote sensing products contaminated by thick clouds and shadows using multitemporal dictionary learning," *IEEE Transactions on Geoscience and Remote Sensing*, vol. 52, pp. 7086–7098, 2014.

[101] W. Freeman, T. Jones, and E. Pasztor, "Example-based super-resolution," *IEEE Computer Graphics and Applications*, vol. 22, no. 2, pp. 56–65, 2002.

[102] Y. Li, D. Sun, X. Zhan, P. Houser, C. Yang, and J. J. Qu, "Downscaling land surface temperature derived from microwave observations with the super-resolution reconstruction method: A case study in the conus," *Remote Sensing*, vol. 16, no. 5, 2024. [Online]. Available: https://www.mdpi.com/2072-4292/16/5/739

[103] Q. Zhou, G. Xian, and H. Shi, "Gap fill of land surface temperature and reflectance products in landsat analysis ready data," *Remote Sensing*, vol. 12, no. 7, 2020. [Online]. Available: https://www.mdpi.com/2072-4292/12/7/1192

[104] A. Mishra, A. Ohri, P. K. Singh, N. Singh, and R. K. Calay, "Improving the prediction of land surface temperature using hyperparameter-tuned machine learning algorithms," *Atmosphere*, vol. 16, no. 11, 2025. [Online]. Available: https://www.mdpi.com/2073-4433/16/11/1295

[105] M. Sarafanov, E. Kazakov, N. O. Nikitin, and A. V. Kalyuzhnaya, "A machine learning approach for remote sensing data gap-filling with open-source implementation: An example regarding land surface temperature, surface albedo and ndvi," *Remote Sensing*, vol. 12, no. 23, 2020. [Online]. Available: https://www.mdpi.com/2072-4292/12/23/3865

[106] N. Arslan and A. Sekertekin, "Application of long short-term memory neural network model for the reconstruction of modis land surface temperature images," *Journal of Atmospheric and Solar-Terrestrial Physics*, vol. 194, p. 105100, 2019. [Online]. Available: https://www.sciencedirect.com/science/article/pii/S1364682619302937

[107] C. Xue, T. Wu, and X. Huang, "Missing data reconstruction in land surface temperature based on the improved u-net framework," in *2021 International Conference of Social Computing and Digital Economy (ICSCDE)*, 2021, pp. 205–210.

[108] Z. Yin, P. Wu, G. M. Foody, Y. Wu, Z. Liu, Y. Du, and F. Ling, "Spatiotemporal fusion of land surface temperature based on a convolutional neural network," *IEEE Transactions on Geoscience and Remote Sensing*, vol. 59, no. 2, pp. 1808–1822, 2021.

[109] R. Li, H. Yang, X. Zhang, X. Xu, L. Shao, and K. Bai, "Near real-time land surface temperature reconstruction from fy-4a satellite using spatio-temporal attention network," *International Journal of Applied Earth Observation and Geoinformation*, vol. 139, p. 104480, 2025. [Online]. Available: https://www.sciencedirect.com/science/article/pii/S156984322500127X

[110] H. Fu, Z. Shao, P. Fu, X. Huang, T. Cheng, and Y. Fan, "Combining atc and 3d-cnn for reconstructing spatially and temporally continuous land surface temperature," *International Journal of Applied Earth Observation and Geoinformation*, vol. 108, p. 102733, 2022. [Online]. Available: https://www.sciencedirect.com/science/article/pii/S0303243422000599

[111] G. Liu, F. A. Reda, K. J. Shih, T. Wang, A. Tao, and B. Catanzaro, "Image inpainting for irregular holes using partial convolutions," *CoRR*, vol. abs/1804.07723, 2018. [Online]. Available: http://arxiv.org/abs/1804.07723

[112] M. Chen, Z. Sun, B. H. Newell, C. A. Corr, and W. Gao, "Missing pixel reconstruction on landsat 8 analysis ready data land surface temperature image patches using source-augmented partial

convolution," *Remote Sensing*, vol. 12, no. 19, 2020. [Online]. Available: https://www.mdpi.com/2072-4292/12/19/3143

[113] F. Huber, S. Schulz, and V. Steinhage, "Deep interpolation of remote sensing land surface temperature data with partial convolutions," *Sensors*, vol. 24, 3 2024.

[114] I. Khedher, J.-M. Favreau, S. Miguet, and G. Gesquière, "A multimodal deep learning approach for high-resolution land surface temperature estimation," in *Applied Soft Computing and Communication Networks*, S. M. Thampi, J. Hu, A. K. Das, J. Mathew, and S. Tripathi, Eds. Singapore: Springer Nature Singapore, 2024, pp. 363–377.

[115] I. Khedher, J.-M. Favreau, S. Miguet, and G. Gesquière, "Rgb2lst: Enhancing deep learning-based land surface temperature estimation with multi-modality and artifacts removal," in *2024 32nd European Signal Processing Conference (EUSIPCO)*, 2024, pp. 2002–2006.

[116] P. Wu, Y. Su, S. bo Duan, X. Li, H. Yang, C. Zeng, X. Ma, Y. Wu, and H. Shen, "A two-step deep learning framework for mapping gapless all-weather land surface temperature using thermal infrared and passive microwave data," *Remote Sensing of Environment*, vol. 277, p. 113070, 2022. [Online]. Available: https://www.sciencedirect.com/science/article/pii/S0034425722001845

[117] M. Jin, "Interpolation of surface radiative temperature measured from polar orbiting satellites to a diurnal cycle: 2. cloudy-pixel treatment," *Journal of Geophysical Research: Atmospheres*, vol. 105, pp. 4061–4076, 2000. [Online]. Available: https://agupubs.onlinelibrary.wiley.com/doi/abs/10.1029/1999JD901088

[118] W. Yu, Y. Li, X. Han, L. Fan, W. Zhou, M. Ma, and W. Shi, *LST Reconstruction on the Remote-Sensed LST Products Under Clouds*. Singapore: Springer Nature Singapore, 2024, pp. 93–116. [Online]. Available: https://doi.org/10.1007/978-981-97-4178-6_6

[119] F. Xu and X. Zhu, "A cloud-regulated land surface warming model to reconstruct daytime surface temperatures under cloudy conditions," *Remote Sensing of Environment*, vol. 328, p. 114873, 2025. [Online]. Available: https://www.sciencedirect.com/science/article/pii/S0034425725002779

[120] O. Güngör Şahin and O. Gündüz, "A novel land surface temperature reconstruction method and its application for downscaling surface soil moisture with machine learning," *Journal of Hydrology*, vol. 634, p. 131051, 2024. [Online]. Available: https://www.sciencedirect.com/science/article/pii/S0022169424004463

[121] C. Shi, T. Wang, S. Wang, A. Jia, X. Zheng, W. Leng, and Y. Du, "Mdineof: A scheme to recover land surface temperatures under cloudy-sky conditions by incorporating radiation fluxes," *Remote Sensing of Environment*, vol. 309, p. 114208, 2024. [Online]. Available: https://www.sciencedirect.com/science/article/pii/S0034425724002268

[122] F. Hong, W. Zhan, F.-M. Göttsche, J. Lai, Z. Liu, L. Hu, P. Fu, F. Huang, J. Li, H. Li, and H. Wu, "A simple yet robust framework to estimate accurate daily mean land surface temperature from thermal observations of tandem polar orbiters," *Remote Sensing of Environment*, vol. 264, p. 112612, 2021. [Online]. Available: https://www.sciencedirect.com/science/article/pii/S0034425721003321

[123] A. Jia, S. Liang, D. Wang, L. Ma, Z. Wang, and S. Xu, "Global hourly, 5 km, all-sky land surface temperature data from 2011 to 2021 based on integrating geostationary and polar-orbiting satellite data," *Earth System Science Data*, vol. 15, no. 2, pp. 869–895, 2023. [Online]. Available: https://essd.copernicus.org/articles/15/869/2023/

[124] P. Yu, T. Zhao, J. Shi, Y. Ran, L. Jia, D. Ji, and H. Xue, "Global spatiotemporally continuous modis land surface temperature dataset," *Scientific Data*, vol. 9, p. 143, 2022. [Online]. Available: https://doi.org/10.1038/s41597-022-01214-8

[125] J. Ma, H. Shen, M. Jiang, L. Lin, C. Meng, C. Zeng, H. Li, and P. Wu, "A mechanism-guided machine learning method for mapping gapless land surface temperature," *Remote Sensing of Environment*, vol. 303, p. 114001, 2024. [Online]. Available: https://www.sciencedirect.com/science/article/pii/S0034425724000129

[126] D. Guo, C. Wang, S. Zang, J. Hua, Z. Lv, and Y. Lin, "Gap-filling of 8-day terra modis daytime land surface temperature in high-latitude cold region with generalized additive models (gam)," *Remote Sensing*, vol. 13, no. 18, 2021. [Online]. Available: https://www.mdpi.com/2072-4292/13/18/3667

[127] A. Dumitrescu, M. Brabec, and S. Cheval, "Statistical gap-filling of seviri land surface temperature," *Remote Sensing*, vol. 12, no. 9, 2020. [Online]. Available: https://www.mdpi.com/2072-4292/12/9/1423

[128] X. Zhang, J. Zhou, S. Liang, and D. Wang, "A practical reanalysis data and thermal infrared remote sensing data merging (rtm) method for reconstruction of a 1-km all-weather land surface temperature," *Remote Sensing of Environment*, vol. 260, p. 112437, 2021. [Online]. Available: https://www.sciencedirect.com/science/article/pii/S0034425721001553

[129] H. Chen, S. Chang, P. He, and C. Zhang, "A machine learning-based method for modis lst downscaling and reconstruction in diverse regions and seasons," in *IGARSS 2024 - 2024 IEEE International Geoscience and Remote Sensing Symposium*, 2024, pp. 9239–9243.

[130] W. Tan, C. Wei, Y. Lu, and D. Xue, "Reconstruction of all-weather daytime and nighttime modis aqua-terra land surface temperature products using an xgboost approach," *Remote Sensing*, vol. 13, no. 22, 2021. [Online]. Available: https://www.mdpi.com/2072-4292/13/22/4723

[131] F. Xu, J. Fan, C. Yang, J. Liu, and X. Zhang, "Reconstructing all-weather daytime land surface temperature based on energy balance considering the cloud radiative effect," *Atmospheric Research*, vol. 279, p. 106397, 2022. [Online]. Available: https://www.sciencedirect.com/science/article/pii/S0169809522003830

[132] H. Zhang, B.-H. Tang, and Z.-L. Li, "A practical two-step framework for all-sky land surface temperature estimation," *Remote Sensing of Environment*, vol. 303, p. 113991, 2024. [Online]. Available: https://www.sciencedirect.com/science/article/pii/S0034425724000026

[133] D. Cho, D. Bae, C. Yoo, J. Im, Y. Lee, and S. Lee, "All-sky 1 km modis land surface temperature reconstruction considering cloud effects based on machine learning," *Remote Sensing*, vol. 14, no. 8, 2022. [Online]. Available: https://www.mdpi.com/2072-4292/14/8/1815

[134] X. Zhang, J. Zhou, S. Liang, L. Chai, D. Wang, and J. Liu, "Estimation of 1-km all-weather remotely sensed land surface temperature based on reconstructed spatial-seamless satellite passive microwave brightness temperature and thermal infrared data," *ISPRS Journal of Photogrammetry and Remote Sensing*, vol. 167, pp. 321–344, 2020. [Online]. Available: https://www.sciencedirect.com/science/article/pii/S092427162030201X

[135] I. Rolland, S. Selvakumaran, S. F. E. Ahmad Shaikh, P. Hamel, and A. Marinoni, "Improving land surface temperature estimation in cloud cover scenarios using graph-based propagation," *Geophysical Research Letters*, vol. 51, no. 23, p. e2024GL108263, 2024. [Online]. Available: https://agupubs.onlinelibrary.wiley.com/doi/abs/10.1029/2024GL108263

[136] Y. Gong, H. Li, H. Shen, C. Meng, and P. Wu, "Cloud-covered modis lst reconstruction by combining assimilation data and remote sensing data through a nonlocality-reinforced network," *International Journal of Applied Earth Observation and Geoinformation*, vol. 117, p. 103195, 2023. [Online]. Available: https://www.sciencedirect.com/science/article/pii/S1569843223000171

[137] K. Kustura, D. Conti, M. Sammer, and M. Riffler, "Harnessing multi-source data and deep learning for high-resolution land surface temperature gap-filling supporting climate change adaptation activities," *Remote Sensing*, vol. 17, no. 2, 2025. [Online]. Available: https://www.mdpi.com/2072-4292/17/2/318

[138] S. Liu, L. Zhang, and S. Wang, "Resolution revolution: A physics-guided deep learning framework for spatiotemporal temperature reconstruction," 2025. [Online]. Available: https://arxiv.org/abs/2507.09872

[139] M. Zhang, Y. Chen, F. Yang, and Z. Qin, "Attention-driven and multi-scale feature integrated approach for earth surface temperature data reconstruction," *EGUsphere*, vol. 2025, pp. 1–25, 2025. [Online]. Available: https://egusphere.copernicus.org/preprints/2025/egusphere-2025-1980/

[140] S. Liu, S. Wang, and L. Zhang, "Daily land surface temperature reconstruction in landsat cross-track areas using deep ensemble learning with uncertainty quantification," 2025. [Online]. Available: https://arxiv.org/abs/2502.14433

[141] J. Guo, J. Quan, W. Zhan, and Z. Wen, "Comparison of gap-filling methods for generating landsat-like land surface temperatures under all-weather conditions," *ISPRS Journal of Photogrammetry and Remote Sensing*, vol. 225, pp. 113–130, 2025. [Online]. Available: https://www.sciencedirect.com/science/article/pii/S0924271625001650

[142] L. Ma, Y. Liu, X. Zhang, Y. Ye, G. Yin, and B. A. Johnson, "Deep learning in remote sensing applications: A meta-analysis and review," *ISPRS Journal of Photogrammetry and Remote Sensing*, vol. 152, pp. 166–177, 2019. [Online]. Available: https://www.sciencedirect.com/science/article/pii/S0924271619301108

[143] L. Chi, B. Jiang, and Y. Mu, "Fast fourier convolution," H. Larochelle, M. Ranzato, R. Hadsell, M. F. Balcan, and H. Lin, Eds., vol. 33. Curran Associates, Inc., 2020, pp. 4479–4488. [Online]. Available: https://proceedings.neurips.cc/paper_files/paper/2020/file/2fd5d41ec6cfab47e32164d5624269b1-Paper.pdf

[144] R. Suvorov, E. Logacheva, A. Mashikhin, A. Remizova, A. Ashukha, A. Silvestrov, N. Kong, H. Goka, K. Park, and V. Lempitsky, "Resolution-robust large mask inpainting with fourier convolutions,"

in *2022 IEEE/CVF Winter Conference on Applications of Computer Vision (WACV)*, 2022, pp. 3172–3182.

[145] N. Bochow, A. Poltronieri, M. Rypdal, and N. Boers, "Reconstructing historical climate fields with deep learning," *Atmospheric science*, 4 2025. [Online]. Available: https://www.science.org/doi/10.1126/sciadv.adp0558

[146] Y. Guo, W. He, Y. Xia, and H. Zhang, "Blind single-image-based thin cloud removal using a cloud perception integrated fast fourier convolutional network," *ISPRS Journal of Photogrammetry and Remote Sensing*, vol. 206, pp. 63–86, 2023. [Online]. Available: https://www.sciencedirect.com/science/article/pii/S0924271623002903